Research Paper

Influence of pin-fin patterns and geometry on the effectiveness of jet impingement boiling – A computational study

L. Ludick [a], K.J. Craig [a,*], P. Valluri [b], J.P. Meyer [a]

[a] Department of Mechanical and Aeronautical Engineering, University of Pretoria, Pretoria, South Africa
[b] Institute for Multiscale Thermofluids, School of Engineering, The University of Edinburgh, Edinburgh, United Kingdom

ARTICLE INFO

ABSTRACT

Jet impingement combined with phase change in the form of boiling has been proven to enhance heat transfer in thermal management applications. When added to surface enhancement, a further increase in heat transfer can be envisaged. Surface enhancement in the form of pin-fins are investigated numerically for a confined single jet of HFE 7100 impinging on a copper surface under boiling conditions. ANSYS Fluent with the Rensselaer Polytechnic Institute boiling model embedded in the Eulerian multiphase framework is utilised. After validating the resulting boiling curve against experiments with an in-line arrangement of pin-fins, a parametric study to investigate the effect of pin geometry, and pattern was performed. Key parameters included Reynolds numbers, pin-fin heights, pin-fin spacing and a star pattern. The objective of the parametric analysis was to limit the dry-out regions in the domain. Finding that local dry-out is decreased through decreasing flow obstruction and heat transfer is mainly linked to surface augmentation. Our results show that for the experimental configuration, 17 % of the pin-fin area experienced dry-out at the 23.2 W/cm² input heat flux. Dry-out was practically eliminated for low pin-fins spaced far apart as expected. But, when keeping the surface augmentation factor constant in a star pattern, the dry-out area was reduced from 17 % to 1 % at the same input heat flux without a significant change in the wall superheat. In addition, the star pattern distribution allowed for a substantial increase in the critical heat flux compared to the in-line arrangement. It was also demonstrated that the pressure drop over the domain was independent of the surface enhancement as it was dominated by the jet stagnation pressure.

1. Introduction

Thermal management of densely packed chips is critical for developing prevailing chips. However, recent developments exceed the heat dissipation capability of conventional single-phase cooling techniques [2]. Therefore, a shift is made towards phase-change cooling techniques to take advantage of the fluid's sensible and latent heat, yielding a much higher heat transfer coefficient [2]. Various multiphase cooling techniques have been performed in literature, including pool boiling, channel flow boiling, spray cooling, boiling jet impingement, and hybrid cooling systems based on a combination of flow boiling and jet impingement [2]. Multiphase jet impingement demonstrates numerous advantages over pool- and flow-boiling techniques as impinging flow actively removes developing vapour, increasing the critical heat flux (CHF) significantly. The heat transfer coefficient (HTC) of jet impingement is significantly affected by liquid properties, domain configurations, and surface structures [3]. Liquid jet impingement configurations

consist of free surface jets, submerged jets and confined jets [4]. Confined impinging jets have the advantage of small-space design [5], making them favourable for cooling electronic devices.

Heat and mass transfer rates are highly enhanced by turbulence [6], and enhancement techniques have gained traction in recent literature, focusing on spent fluid removal, fluid investigations and surface enhancements. Cui *et al.* [7] investigated the effect of spent fluid removal and surface enhancements and found that heat transfer is enhanced if jet crossflow is eliminated through the use of effusion holes. Devahdhanush and Mudawar [8] investigated submerged boiling jet impingement using R134a operating in a heat flux range between 20 W/cm^2 and 220 W/cm^2 at 7.5 bar. Katto and Kunihiro experimented [9] with water reaching heat fluxes as high as 280 W/cm^2. HFE fluids have gained traction in recent years [1,7,10–12] due to their high surface wettability, low boiling point at 1 atm and high dielectric strength [1]. Pranoto *et al.* [13] reached heat fluxes of 26 W/cm^2 to 30 W/cm^2 for pool boiling whilst using HFE 7100 at 1 atm on micropillar surfaces. Ji *et al.* [12] and Cheng *et al.* [14] also used HFE 7100 on micropillars and reached heat fluxes up

---

Nomenclature

A	Area, m^2
C	Correlation constant,-
Cp	Constant pressure specific heat capacity, $J/(kg \bullet K)$
d	Bubble diameter, m
d_h	long axis of the deformable bubble
E	Near-wall treatment constant,-
F	Force, N
f	Drag force function,-
G	Production of turbulent kinetic energy, $kg/m \bullet s^3$
h_{fg}	Latent heat of vaporization, J/kg
J	Diffusive heat flux, W/m^2
Ja	Jacob number,-
k	Turbulent kinetic energy, m^2/s^2
K,m	Empirical constants,-
L	Length, m
$\dot{m}$	Mass flow rate, kg/s
Nu	Nusselt number,-
N	Number of jets,-
Pr	Prandtl number,-
P	Pressure, Pa
$q^{\bullet\bullet}$	Heat flux, W/m^2
Q	Heat exchange, W/m^3
Ra	Surface roughness, μm
Re	Reynolds number,-
R_ε	RNG additional term,-
r/D	Radial distribution,-
R	Interaction Force, N
S	Source term in turbulence and energy equations,-
t	time, s
T	Period, s^{-1}
T	Temperature, K
V	Volume, m^3
v	velocity, m/s
y	Perpendicular distance from wall, m
y_v	Physical viscous sublayer,-
y_v^*	Viscous sublayer constant,-

Greek symbols

α	Volume fraction
δ	Boundary layer region
ε	Turbulent dissipation rate
η	Surface efficiency
λ	Phase diffusivity, m^2/s
μ	Dynamic viscosity, $Pa \bullet s$
ν	Kinematic viscosity, m^2/s
ρ	Density, kg/m^3
$\sigma_{\varepsilon,m}$	Inverse of the effective Prandtl number,-
τ	Shear stress, Pa
κ	Thermal conductivity, $W/(m \bullet K)$

Subscripts

aw	Adiabatic wall
b	bulk
b	Buoyancy
c	Convection
c	corrected
cp	Contact pressure
$crit$	Critical bubble diameter
d	Drag
D	Drag coefficient
du	Asymmetric growth
E	Evaporative heat flux
eff	Effective
f	fins
fl	fluid
h	Hydrostatic pressure
i	Inertia
$Lift$	Lift coefficient
ls	Liquid saturated
m	mixture
o	Overall
p	Phase p
p	pressure
$part$	particle
q	Phase q
Q	Quench
ref	Reference
s	Solid
s	Surface tension
sat	Saturated
sub	Subcooled
TD	Turbulent dispersion
vm	Virtual mass coefficeint
w,W	Wall
wl	Wall lubrication
wt	Waiting time
$Eo^{\grave{}}$	modified Eötvös number
i	Interfacial area concentration
x_e	Thermodynamic equilibrium

Superscripts

n	Lemmert and Chawla empirical coefficient

Acronyms and abbreviations

AMG	Algebraic multigrid
CFD	Computational Fluid Dynamics
CFL	Courant Friedrichs Lewy
CHF	Critical heat flux
HFE	Hydrofluorether
HTC	Heat transfer coefficient
OND	Onset of nucleate boiling
PCB	Printed circuit boards
PEEK	Polyether ether ketone
PRESTO!	PREssure Staggering Option
RNG	Renormalization group methods
RPI	Rensselaer Polytechnic Institute
SIMPLE	The Semi-Implicit Method for Pressure-Linked Equations
UDF	User defined function

to 280 W/cm^2 with an array of jets with 40–41 degrees of subcooling. A rapid increase in the gradient of the boiling curve can be expected after the onset of nucleation boiling (ONB) due to the fast bubble growth and departure of HFE fluids, causing a latent heat release [15]. In recent years, the same results are gained through the use of nanofluids by modifying the mean properties of the base fluid, ultimately improving bubble dynamics and formation [16]. For instance, Song *et al.* [17] improved the heated surface with the deposition of a GNP/Ag mixed nanofluid and a GNP-Ag hybrid nanofluid and observed a significant increase in heat transfer compared to a bare copper surface. The formation of a fluffy and porous surface facilitates the lateral heat transfer of the heating surface by increasing the vaporization core to promote

bubble separation [18,19], as also reported by Rau *et al.* [1] with the inclusion of a microporous layer on a pin-finned surface. Furthermore, Xu Ma *et al.* [20] found that the use of GNP $-Fe_3O_4$ hybrid nanoparticles increase wettability, reduced the bubble generation period and resulted in smaller bubble detachment diameters, thereby prolonging the CHF. This enhancement technique is further emphasised in a study by Xu Ma *et al.* [21]. These findings collectively highlight the potential of nanofluid to decrease local dry-out regions.

Surface enhancements increase the product of average surface heat transfer coefficient and surface area by disrupting boundary layer growth and improving turbulent transport [22]. Feng *et al.* [15] studied the flow boiling characteristics of microchannels with various pillar distributions. As a result, bubble nucleation, slug liquid film, and local dry-out are identified as the three distinct boiling regions between pillars throughout the boiling curve. Liquid film evaporation is critical in heat transfer enhancements [15]. However, completely evaporating the liquid film will lead to local dry-out, deteriorating heat transfer and damaging the surface. Qiu *et al.* [23] investigated experimentally and numerically the boiling heat transfer in a chamber with staggered pillars. The densely packed pillars obstructed flow, creating large wakes and accumulating vapour in the downstream regions.

Wan *et al.* [24] studied the effect of pin-fin shapes in flow boiling. They found that the pin-fin shape has a negligible effect on the initiation of the ONB, as the ONB is triggered for all shapes at approximately the same wall superheat. The liquid film formation is consistent with various fin shapes and distributions. However, pin-fin shape and formation influenced the commencement point of local dry-out on the boiling curve.

Rau *et al.* [1] and Ndao *et al.* [22] performed boiling single jet impingement experiments on microstructured surfaces, concluding that microstructured surfaces produce a higher heat transfer coefficient than flat surfaces. Apart from using grooved surfaces, Jenkins *et al.* [25] gained the same increase in heat transfer coefficient. Rau *et al.* [1] attributed the reduction in heat transfer performance at high heat fluxes to dry out at the base of the fins. A similar trend was experienced by Feng *et al.* [15] with horizontal flow boiling.

Local dry-out is a consequence of stagnating flow initiated by flow obstruction. Fig. 1 (a) depicts the liquid velocity distribution of a single jet impinging on a confined surface populated with a uniform distribution of inline pin-fins (figure taken from the results section of this study described in section 4.4). The liquid flow distribution in the pin-fin vicinity forms a cross through the centre of the heated block as the uniform pattern of the fins allows liquid to flow along the channels perpendicular to the impingement periphery. Conversely, a compact staggered arrangement obstructs flow from advancing towards the edges of the heated block, creating stagnant flow regions at the edge of the heated block. Fig. 1 (b) depicts the spatial distribution of the local boiling type,

comprising pool boiling (at the outer regions of the domain and in the wake of each pin-fin), flow boiling, and, convection and quenching at the jet stagnation region as liquid actively removes evaporation bubbles. The effect of pin-fin layout and distribution on the total heat transfer coefficient and local dry-out remains an unanswered question in boiling jet impingement, which this paper aims to provide insight into.

Numerical simulations of two-phase flow boiling remain challenging and complex, and few numerical investigations on boiling jet impingement exist in literature. Narumanchi *et al.* [26] explored the nucleate boiling regime numerically through a 2D axisymmetric domain. Abished *et al.* [27] and Esmailpour *et al.* [28], investigated the effect of controlling parameters such as jet Reynolds number, degree of subcooling, and jet-to-target spacing. Subsequent work by Qiu *et al.* [29] incorporated thermal mass or conjugation in the study of a single axisymmetric jet. In all these cases, heat transfer was predicted using the Eulerian multiphase framework incorporating the Rensselaer Polytechnic Institute (RPI) boiling model. Finally, Wright *et al.* [30] extended numerical investigations to 3D jet arrays and highlighted the importance of including conjugation should the heated scheme in the experimental setup consist of a large thermal mass. However, all of the above numerical works of perpendicular jet impingement boiling are limited to flat surfaces without any surface augmentation. The inclusion of structured surfaces on boiling jet impingement further increases numerical complexity due to the different boiling types depicted in Fig. 1 (b).

Previous numerical work demonstrated that the Eulerian multiphase framework incorporated with the RPI boiling model could accurately predict heat transfer in boiling jet impingement. However, the integration of conjugate heat transfer is essential due to the high thermal gradient formed by the impinging jet and structured surfaces. The current study aims to validate a single jet on pin-fin surfaces, analyse the effect of local dry-out due to the structured surfaces and perform a parametric analysis using the pin-fins' dimensions, pitch and configuration, as parameters. The analysis intends to maximise heat transfer through surface augmentation but eliminate local dry-out to reduce microchip damage in boiling jet impingement.

Section 2 defines the problem statement i.e. a 3D surface that is subjected to a single jet, followed by the numerical framework in Section 3. Section 4 presents the numerical validation of a single jet impinging on pin-fin surfaces against existing experimental results from literature. A parametric study presented in Section 5 investigates the effect of inlet Reynolds number, pin-fin dimensions, pitch, and distribution. Finally, Section 6 details the key conclusions drawn.

2. Problem definitions and numerical modelling methodology

In this section, we describe the problem of a 3D pin-fin surface subjected to a single jet simulating experiments of Rau and Garimella
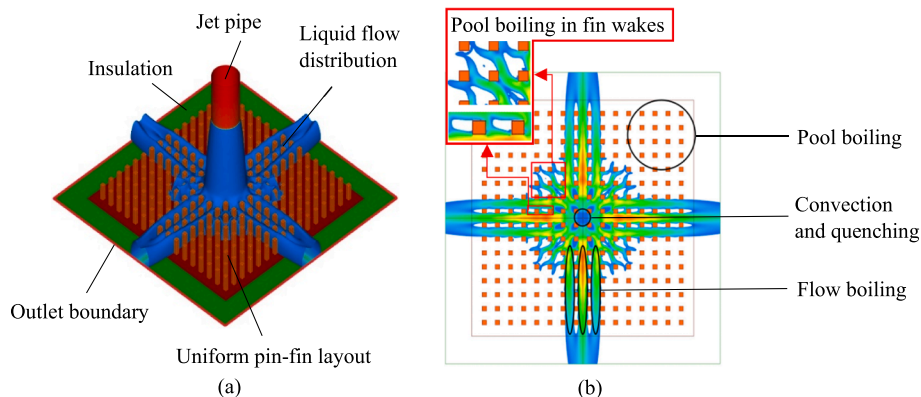

Fig. 1. (a) Iso surface of liquid velocity > 0.3 m/s distribution of a single jet impinging on a pin-finned surface (b) Spatial distribution of local boiling type along a uniformed pin-fin distribution.

[1]. We also present the modelling and numerical method used.

2.1. 3D pin-fin surface subjected to a single jet

The experiments of Rau and Garimella [1] investigated the effect of structured surfaces in the form of pin-fins in boiling jet impingement using the dielectric working fluid HFE-7100. The heat transfer performance of a confined, single 3.75 mm jet is compared on various surfaces, including a smooth flat surface, a macroscale pin–fin surface and a hybrid combination of a flat surface with a microporous coating and a pin–fin surface with a microporous coating. In the current computational study, we only consider the macroscale pin–fin surface. Fig. 2 illustrates the chosen computational domain on the experimental setup of Rau and Garimella [1], further illustrated in Fig. 3. It was found that extending the domain radially had a negligible influence (1 %) on the reported wall superheat at the stagnation point, and no influence on the single-phase flow patterns in the region of interest and caused a limited modification of the vapour formation during heating. This results of this extended domain (not shown here) motivated the use of the chosen computational domain.

Only a quarter of the domain is modelled as a symmetry plane can be drawn to divide the domain into four symmetrical counterparts. As a result, a quarter model obtains the same level of accuracy whilst decreasing the computational costs, under the assumption that the vapour formation is symmetric as well. A velocity inlet is defined at the top of the orifice plate, normal to the longitudinal axis of the opening in the orifice plate. The orifice plate's internal and bottom boundary is defined as an adiabatic wall. Coupled walls are defined between the adjoining copper block, insulation, and fluid. The outside walls of the insulation are also defined as adiabatic walls. Considering an extended upstream domain had a negligible difference in the stagnation temperature. The pressure drop over the stagnating jet was simulated to be within 1 % of the value reported in Fig. 10 of Rau and Garimella [1]. A hydrostatic pressure gradient is added to the pressure outlet to account for the added hydrostatic pressure caused by the bulk fluid during evaporation [30]. The wetted surface area consists of 256 CNC-machined 0.5 mm × 0.5 mm × 2.5 mm pin-fins uniformly and inline distributed over the square wetted surface with a pitch of 1.5 mm. The design objective of the pin-fins involves a significant surface augmentation whilst preserving adequate spacing for fluid to flow past [1]. Finally, uniform heat flux is applied at the bottom of the copper block with polyether ether ketone (PEEK) surrounding the copper block to act as insulation.
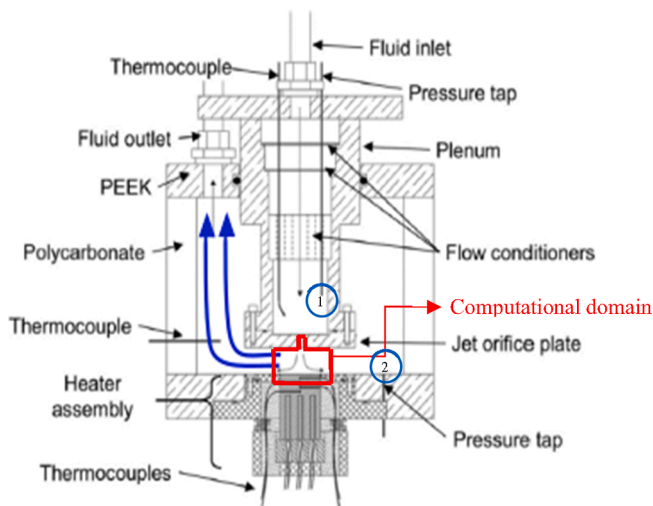

Fig. 2. Computational domain location on the experimental setup of Rau and Garimella. Pressure tap locations indicated. [1].

3. Modelling

3.1. Numerical framework

A commercial CFD software, Ansys Fluent 2022 R2, was used to model subcooled boiling jet impingement on enhanced surfaces. The numerical framework follows the same outline as Wright *et al.* [30]. A transient, Euler-Euler approach was used as the foundation of the numerical model, with liquid as the primary phase and vapour as the dispersed phase. Conjugate heat transfer was predicted through the Rensselaer Polytechnic Institute (RPI) wall-boiling model, which is embedded in the Eulerian multiphase model. Multiphase flows are treated as interpenetrating continua where volume fractions represent the space of each phase occupied in a control volume. The numerical framework used in this study is outlined in Appendix A with multiphase turbulence modelled through the renormalisation (RNG) $k - \varepsilon$ mixture turbulence model, where an additional source term is added to the turbulence dissipation equation to account for the dispersed phase-induced turbulence and the differences between the production and destruction thereof.

The accuracy of numerical solutions is significantly impacted through near-wall modelling as walls act as the primary source of turbulence and vorticity. In the case of complex flows involving separation, reattachment, and impingement where the turbulence and the mean flow are subjected to pressure gradients, and rapid changes, a two-layer-based, non-equilibrium wall function [31] is used rather than standard wall functions. This is due to the fact that the assumption of local equilibrium is no longer valid as the production of turbulent kinetic energy is no longer equal to the destruction thereof, which is neglected in the standard wall functions.

3.2. Near wall treatment

The non-equilibrium wall functions remain partly the same as standard wall functions, but the log-law for mean velocity is sensitised to pressure gradients by formulating a y^* insensitive near-wall function. If flow separation occurs, $\tau_w \to 0$, collapsing the y^+ formulation. Thus, the introduction of y^* eliminated the possibility of a collapse [32]. The sensitised velocity is expressed as.

$$\frac{\widetilde{U} C_\mu^{1/4} k^{1/2}}{\tau_w / \rho_p} = \frac{1}{\kappa_p} \ln\left(E \frac{\rho_p C_\mu^{1/4} k^{1/2} y}{\mu_p} \right) \tag{1}$$

where C_μ is a model constant, k the turbulent kinetic energy, τ_w the shear stress at the wall, ρ_p, μ_p and κ_p the density, dynamic viscosity and thermal conductivity at the wall adjacent cell centre, E an empirical constant which is a function of wall roughness, y the normal distance of the centre of the first cell, and

$$\widetilde{U} = U - \frac{1}{2}\frac{dp}{dx}\left[\frac{y_v}{\rho \kappa_p \sqrt{k}} \ln\left(\frac{y}{y_v}\right) + \frac{y - y_v}{\rho_p \kappa_p \sqrt{k}} + \frac{y_v^2}{\mu_p} \right] \tag{2}$$

where $\frac{dp}{dx}$ is the pressure gradient in the wall-normal direction, y_v is the physical viscous sublayer thickness and computed as

$$y_v \equiv \frac{\mu_p y_v^*}{\rho_p C_\mu^{1/4} k_p^{1/2}} \tag{3}$$

where $y_v^* = 11.225$ and k_p is the turbulent kinetic energy at the cell centre. Wall neighbouring cells are assumed to consist of a viscous sublayer and a fully turbulent layer. The following assumptions are made to calculate the turbulent quantities:

$$\tau_t = \begin{cases} 0, & y < y_v \\ \tau_w, & y > y_v \end{cases} \tag{4}$$
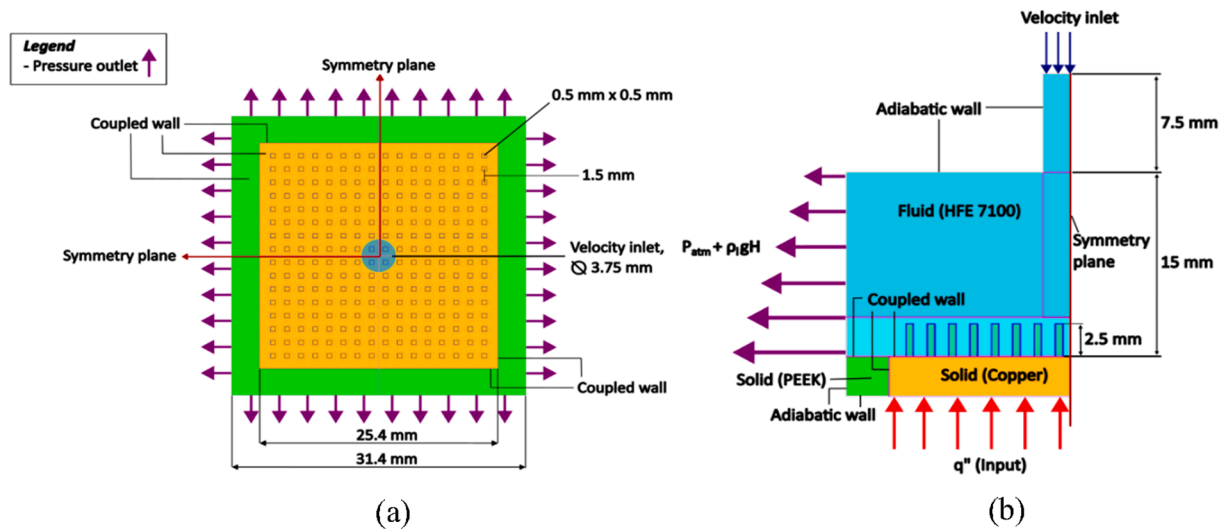
Fig. 3. Computational domain of a single jet on pin-fins (a) top view and (b) symmetry plane side view, including the effects of conjugation.

$$k = \begin{cases} \left(\frac{y}{y_v}\right)^2 k_p, & y < y_v \\ k_p, & y < y_v \end{cases} \tag{5}$$

$$\varepsilon = \begin{cases} \frac{2 v_m k}{y^2}, & y < y_v \\ \frac{k^{3/2}}{c_l^* y}, & y > y_v \end{cases} \tag{6}$$

where $C_l^* = \kappa_p C_u^{-\frac{3}{4}}$ and v_m the mixture velocity. Through the use of the above quantities, the cell-averaged production of k, G_k and dissipation rate ε can be computed from the volume average of G_k and ε at wall-adjacent cells and for hexahedral cells expressed as

$$G_k \equiv \frac{1}{y_n} \int_0^{y_n} \tau_t \frac{\partial v}{\partial y} dy \tag{7}$$

and

$$\varepsilon = \frac{1}{y_n} \int_0^{y_n} \varepsilon dy \tag{8}$$

where y_n is the height of the cell. The appropriate cell volume averages are used for different cells.

3.3. Solution method

A pressure-based solver is implemented with the phased-coupled SIMPLE scheme for pressure–velocity coupling [32]. The Semi-Implicit Method for Pressure-Linked Equations (SIMPLE) algorithm is an iterative method that obtains an initial guess for the pressure field and solves the discretised momentum equations using the guessed pressure field. First, a correction term is added to the resulting face flux if it does not satisfy the continuity equation. Then, the corrected face flux is used to solve a pressure correction which is in turn used to correct the pressure field and face flux. Finally, all other discretised transport equations are solved from the resulting pressure and face flux—all variables are checked for convergence through comparison with the initial values. If one variable does not satisfy the convergence criteria, all final values are used as initial values to repeat the above iteration. An algebraic multi-grid (AMG) solver enhances convergence and cuts computational costs. An AMG solver is particularly attractive for unstructured meshes as coarser-level equations are not generated through a change in geometry or re-discretisation.

Spatial discretization was achieved through the first-order upwind method. However, the numerical discretization error is increased in the case of complex flows where the flow crosses the mesh lines obliquely. More accurate results can be obtained through second-order discretization, but first-order discretization improves convergence and computational costs. The PREssure STaggering Option (PRESTO!) is used to determine the "staggered" pressures through the use of the discrete continuity balance for a "staggered" control volume. The Least Squares Cell-Based Gradient evaluation is used for constructing values of a scalar at cell faces and computing secondary diffusion terms and velocity derivatives. The Least Squares Cell-Based averaging scheme is known to be as accurate as the node-based gradient method for unstructured meshes. However, it is found to be less expensive to compute compared to the node-based method. Warped-face gradient correction is implemented to improve gradient accuracy, especially in meshes with a significant difference in the volume of neighbouring cells. Finally, the first-order implicit formulation is used to achieve time discretization. The implicit formulation is unconditionally stable and allows for a much larger time step size than the explicit formulation. Implicit formulations were used to solve the body forces and the volume fractions.

Due to a coarse mesh and a few poor cells in the pin-fin vicinity, a truncated virtual mass force value was used to enhance convergence. On the other hand, cells that experience a high vapour velocity are prone to cause divergence. Thus, an automatic mesh adaption scheme was formulated to refine cells with an abnormally high vapour velocity leading to better convergence in the targeted cells. In addition, a numerical noise filter was applied to the energy equation to filter out noise due to the fluctuations caused in heat transfer by the drastic change in fluid density and thermal properties at the wall in the phase change process.

All data presented in the following chapters are time-averaged values after a case reached a steady state and the total heat transfer rate into the fluid equalled the total heat transfer rate into the solid.

4. Validation against experiment

In this section, we validate the numerical model against the published results of experimental studies conducted by Rau and Garimella [1] of a confined, single, subcooled jet subjected to a surface consisting of a uniform, inline array of pin-fins.

4.1. Experimental procedure [1] and test module

A closed-loop experimental facility was utilised to recirculate flow

through the jet impingement test section [10]. The test section for confined and submerged jet impingement was assembled with polyether ether ketone (PEEK) and polycarbonate to mitigate heat loss and allow visual observation [10]. The heater assembly consists of a copper block and provides a 25.4 mm × 25.4 mm wetted surface area [1]. A 4 mm-thick PEEK capping plate is sealed around the copper block with four spring-loaded screws to finely adjust the level between the copper block and the capping plate. Twelve 25.4 mm long, 36 Ω cartridge heaters are embedded in the copper block to act as a uniformly distributed heat source. Four T-type sheathed thermocouples are placed inline at the centreline of the block, spaced 2.54 mm apart to measure the centreline temperature, allowing for the surface temperature's extrapolation. The measurement of the centreline temperature only allows the experiments to measure the temperature at the stagnation region, neglecting the surface temperature at the outer regions of the domain. Thus, it is recommended that the average surface temperature is measured as in Devahdhanush and Mudawar [2].

Table 1 includes all operating conditions for flat and pin-fin surfaces at a single flow rate. The experimental investigation used three different flow rates (400, 900, and 1 800 ml/min). However, the highest flow rate was chosen to ensure a fully turbulent flow and serve as a validation case for the present study.

The reported maximum uncertainty for all pressure transducer and thermocouple measurements resulted in $\pm 0.13 kPa$ and ± 0.3 °C bands, respectively. Surface temperature extrapolation resulted in a reported uncertainty of ± 0.4 °C at low heat fluxes and ± 0.8 °C at a heat flux of 88 W/cm^2 [16]. The determination of local heat fluxes is not possible due to the copper block heat source used. Through a standard uncertainty analysis, including uncertainty contributions from the power dissipated from the cartridge heaters, extrapolated surface temperature, and heat loss calculated in ANSYS Fluent [32], the uncertainty in reported experimental heat flux is estimated to be less than 2 %.

4.2. Computational properties and boundary conditions

In the present study, liquid enters the domain at 2.716 m/s at a pressure of 101 325 Pa and a temperature of 51 °C. Constant solid material properties are used for the Copper block and the PEEK insulation (see Table 2). Table 3 includes the fluid properties of the working fluid HFE 7 100. The liquid properties are constant at 51 °C and 1 atm, and the vapour properties are constant as a saturated vapour at 61 °C and 1 atm. All fluid properties are gained through multiple sources, including ([33,13,1]).

Table 4 includes the inlet and outlet conditions of the 3D quarter symmetry domain. Turbulence intensity is left at the Fluent default of 5 %. Outlet backflow conditions are set to allow for liquid and vapour to recirculate from neighbouring cells.

4.3. Mesh independence

Divisions depicted in Fig. 3 (b) illustrate the domain division to allow for a higher-quality mesh. The constant-mesh size was enforced in the jet and fin regions, whilst the mesh grew with a maximum of 20 % in the

Table 1
Operating conditions of confined jet impingement with boiling on flat and pin-fin surfaces [1].

Parameter	Value
Jet diameter [mm]	3.75
Orifice thickness [mm]	7.5
Jet to target spacing [mm]	15
Jet flow rate [ml/min]	1 800
Jet Reynolds number	38 900
Jet velocity [m/s]	2.716
Inlet temperature [°C]	51
Test section pressure [Pa]	101 345

Table 2
Solid material properties at 25 °C.

Property	Copper [32]	PEEK [32]
Density [kg/m^3]	8 978	1 310
Specific heat [$J/(kgK)$]	381	1 340
Thermal Conductivity [$W/(mK)$]	387.6	0.2498

Table 3
Fluid properties.

Fluid	HFE 7100		
Saturation pressure [Pa]	101 325		
Saturation temperature [°C]	61		
Surface tension [N/m]	0.0111027		
	Liquid		Vapour
Temperature [°C]	25	51	61
Density [kg/m^3]	1 481	1 444.34	9.12008
Specific heat [$J/(kg*K)$]	1 183	1 141.86	938.43
Thermal Conductivity [$W/(m*K)$]	6.9 e-02	8.996 e-02	1.4096 e-02
Dynamic viscosity [$kg/(m*s)$]	5.63 e-04	4.195 e-04	1.1409e-05
Molecular Weight [$kg/kmol$]	250.064		
Latent heat [kJ/kg]	111.7		

Table 4
Inlet and outlet conditions of a quarter symmetry domain based on an experiment done by Rau and Garimella [1].

Inlet boundary conditions	
Phase	Liquid
Temperature [°C]	51
Turbulence intensity [%]	5
Outlet boundary conditions	
Backflow phase	Mixture
Backflow turbulence intensity [%]	5
Backflow vapour fraction	From neighbouring cell

bulk fluid region. This mesh study aimed to decrease the mesh density between the fins with a minimum allowable refinement of five cells between fins. Polyhedral and hexahedral cells were used to compare mesh types at the same mesh density. The maximum cell aspect ratio is kept below 8, whilst the minimum cell orthogonality is kept above 0.5 for both polyhedral and hexahedral cells. In addition, automatic mesh adaption was enabled to allow for automatic mesh refinement in possible unstable cells, identified as cells with a vapour velocity five times higher than the inlet velocity. All computations are done at a uniform heat flux input of 23.24 W/cm^2 and a fixed time step of 0.0001 s. The maximum CFL number is kept under 5 for all cases as Ansys Fluent is able to sustain CFL numbers>1 [34]It is also important to note that the implicit method used in the current transient simulation is unconditionally stable [35].

Various factors contributed to the mesh density study, including cell and node density, stagnation region temperature, area-weighted average base wall temperature, dry-out area percentage on the base wall, and nucleation boiling area percentage on the base wall. The stagnation region temperature is calculated through an area-weighted average of 10 % of the jet diameter centred on the longitudinal axis of the jet inlet. The dry-out and fully developed nucleation boiling area percentages are defined as the portions of the base surface area between the fins, excluding the fins tops, experiencing an evaporative heat flux contribution in a cell above 95 %, and between 50 % and 95 %, respectively of the total wall heat flux. The total wall heat flux is calculated from the RPI wall boiling model established by Kurul and Podowski [11], consisting of three components, and is expressed as.

$$\dot{q}_W = \dot{q}_C + \dot{q}_Q + \dot{q}_E \qquad (9)$$

where $\dot{q}_C$ relates to the convective heat flux, $\dot{q}_Q$ to the quenching heat

flux and $\dot{q}_E$ to the evaporative heat flux.

Fig. 4 compares the predicted stagnation temperatures between polyhedral and hexahedral mesh types as a function of the number of cells between fins. A mesh refinement led to both types converging to the same stagnation temperature. Both hexahedral and polyhedral fine meshes produced accurate results with an error of 9.5−9.9 % when considering the upper limit of the experimental stagnation superheat uncertainty. Thus, further investigation only considers the fine mesh cases of 8 cells between the fins as 10 cells between the fins is to computationally expensive for the small gain in accuracy. The fine mesh cases consisted of an initial cell density of 866 $cells/mm^3$ for the polyhedral mesh and 395 $cells/mm^3$ for the hexahedral mesh. The decrease in stagnation temperature with mesh refinement can be due to better-resolved turbulent flow in the pin-fin vicinity, increasing mixing. The wall distance of the first cell can also lead to variable wall temperatures. y^+ gives a reasonable estimate of the required first boundary layer height, but due to the complexity of the flow and mesh in the pin-fin vicinity, y^+ is no longer a helpful tool.

Plots of both the dry-out area contribution and fully developed nucleation boiling area contribution led to cyclic behaviour over time (see Fig. 5 (a) and (b)). The cyclic behaviour is due to the formation and coalescence of vapour columns at the outer regions of the domain (as detailed in the results section), followed by the ability of the liquid to rewet the surface. Rau and Garimella [1] visualised the cyclic process in their experiment, while Qiu et al. [23], although not reported to be cyclic, picked up similar "dry-out" areas with high vapour contributions in stagnant flow regions.

Extractions in Fig. 5 (a) and (b) depict the respective boiling contribution on the base surface at the peak, average and minimum with the dry-out area contribution (red) and fully developed nucleation boiling contribution (purple). The horizontal dashed lines in Fig. 5 (a) and (b) represent the respective average values gained from each graph. A contrary behaviour of the dry-out and nucleate boiling area contributions is found as the decrease in the dry-out area contribution increases the nucleation boiling area contribution and contrariwise. The difference between the polyhedral and hexahedral results was negligible in the dry-out area contribution. On the other hand, results showed a more significant difference in the nucleate boiling area contribution, whereas the hexahedral cells predict a 6.7 % higher average nucleate boiling contribution. Similar results are gained for both fine polyhedral and fine hexahedral cases. Hexahedral cells are the preferred meshing method due to the reduction in computational costs, although, in this study, all further investigations are done with a polyhedral mesh due to software availability.

4.4. Validation

4.4.1. Boiling curve validation

Fig. 6 compares the current results to the boiling curve of Rau and Garimella [1] concerning a confined single jet impinging on a uniform pin-fin layout. Horizontal and vertical uncertainty bars depict the experimental uncertainty of the wall superheat and the heat flux, respectively. Including experimental uncertainties, the simulation error just after the ONB is between 5.2 % and 9.3 %, whilst the error increases to 12.4 % at the highest simulated heat flux. Fig. 6 only represents the stagnation wall temperature (in order to compare directly with the experimental temperature measurement location) and does not reflect any detrimental effects due to local dry-out throughout the domain. Significant local dry-out at a heat flux of $30W/cm^2$ lead to numerical instabilities as the RPI boiling model is developed for the fully-developed nucleation boiling regime. Using HFE-7000 as a working fluid for flow boiling through microstructures, Feng et al. [15] experienced local dry-out at approximately $30W/cm^2$. Pranoto et al. [13] encounterd a similar phenomenon in pool boiling with the working fluid of HFE-7100. Thus, the RPI boiling model cannot be fully trusted at higher heat fluxes as the standard RPI boiling model cannot simulate post dry-out conditions, leading to a larger error at higher fluxes. Heat transfer throughout the boiling curve is underpredicted as each simulated result predicts a higher wall superheat than the experimental results. Underprediction of heat transfer is preferred as an over-prediction of heat transfer will lead to lower simulated wall superheats and may be detrimental to the surface as the actual wall superheat may be higher than the predicted wall superheat.

Narumanchi et al. [26] reported that errors of up to 30 % are acceptable for jet impingement boiling. Wright et al. [30] reported slightly smaller errors of up to 21 % with an overprediction of the onset of nucleate boiling departure. The overprediction was attributed to the fact that the standard RPI boiling model is only applicable in the fully developed nucleate-boiling regime and that the Cole bubble departure frequency model was not applicable for highly subcooled boiling.

The RNG $k−\epsilon$ model shows substantial improvements over the standard $k−\epsilon$ models, where the RNG theory provides an analytically-derived differential formula for effective viscosity that accounts for low Reynolds number effects [32]. Hence, the success of the comparison can be attributed to the ability of the RNG $k−\epsilon$ model to capture the complex multiphase flow patterns throughout the domain. The small deviation in Fig. 5 can also be attributed to the ability of the non-equilibrium near-wall treatment in conjunction with a fine mesh to resolve the constant production and dissipation of turbulence between the fins subjected to severe pressure gradients.

The use of constant liquid properties in the current study also affects the predicted wall superheat. Due to the high degree of subcooling (10 °C), the authors believe that using non-constant properties instead
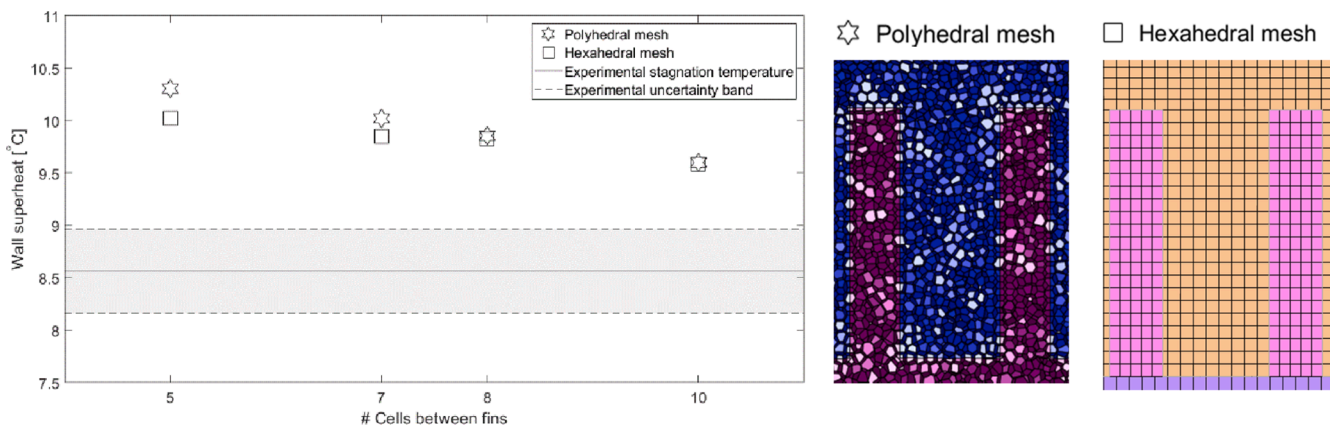

Fig. 4. Mesh independence study: Stagnation wall superheat comparison (left). Visual presentation of mesh types between fins (right).
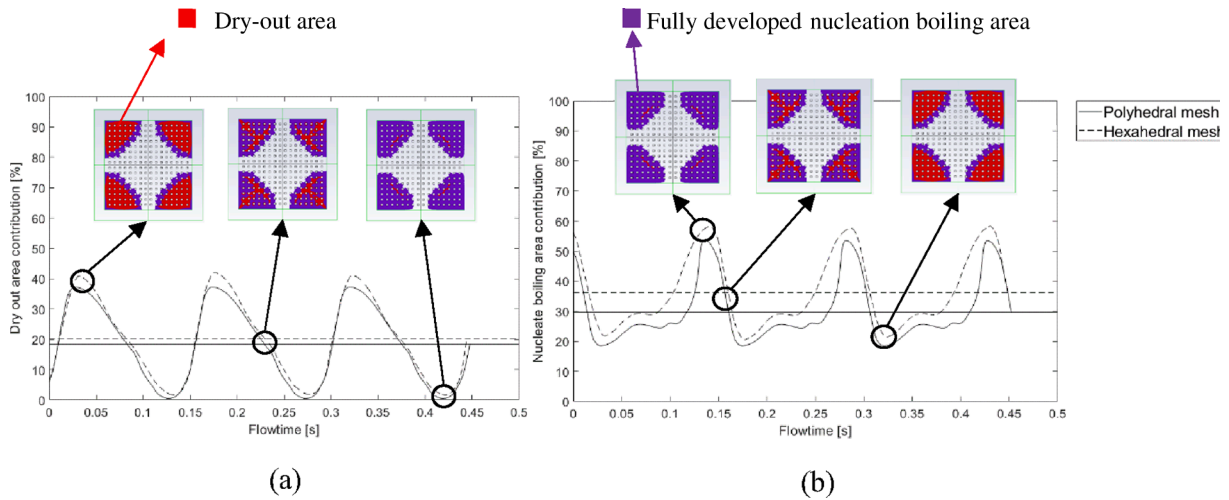
Fig. 5. Mesh independence study: (a) dry-out area contribution on base surface and (b) fully developed nucleation boiling area contribution on base surface.
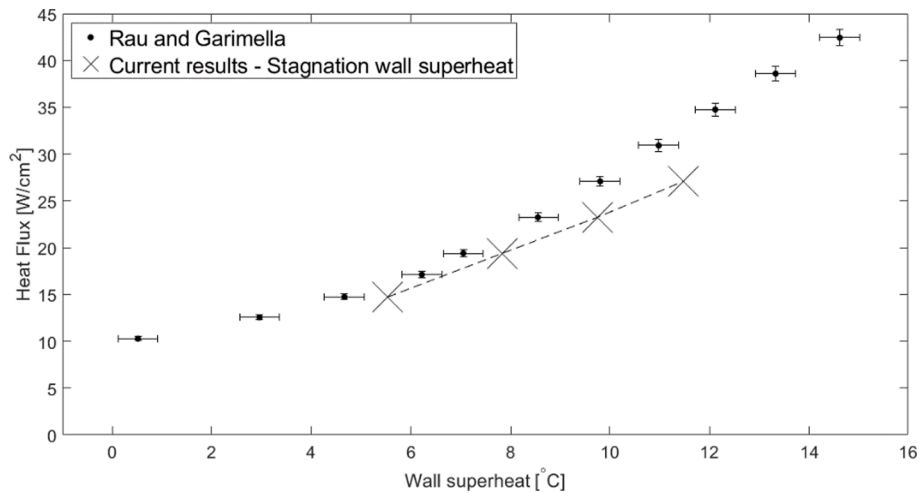

Fig. 6. Boiling curve validation of numerical model against the experiment of Rau and Garimella [1] using the stagnation wall superheat.

would have increased the simulation error as liquid properties at a temperature higher than 51 °C will decrease the heat transfer ability of the liquid.

4.4.2. Total heat rate

Fig. 7 depicts the total heat rate extracted by the fluid compared to the total heat rate applied to the solid (right axis), as linked to the resulting stagnation wall superheat (left axis). The liquid velocity distribution is allowed to develop fully throughout the domain and reach a steady state before the initial heat flux is applied to the solid. Each successively ramped heat flux is then allowed to reach a steady state initially through a ten-second time window, whereas, afterwards, the window is reduced as a steady state is reached in a shorter time window. The first heat flux did not reach a steady state and is not used in
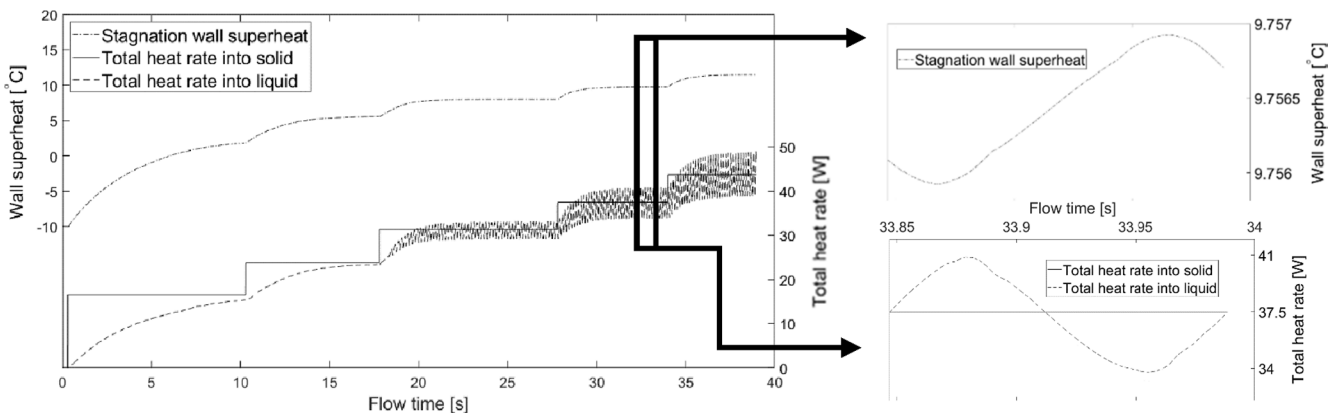

Fig. 7. Stagnation wall superheat and total heat rate vs simulation flowtime.

comparing the results. Thus, the initial heat flux needs a larger time window to reach a steady state. As the second heat flux reaches a steady state, the following heat flux is applied as the total heat rate at the first and second heat flux plateaued without any noise. As the heat flux increased, the initial gradient of the total heat rate into the liquid increased along with the amplitude of oscillations. The boiling model is already active at an input heat flux of 14.7 W/cm^2 However, a steady state is reached without significant oscillations in the total heat rate into the fluid. Oscillations in the total heat rate into the fluid arise at higher heat fluxes (As shown in Fig. 7, to be explored in more detail later). The stagnation wall superheat shows a similar trend as the total heat output graph, with an initial sharp increase in temperature followed by an asymptotic approach towards a steady state. Slight oscillations are present at higher heat fluxes (Shown in Fig. 7) but are insignificant compared to the total heat rate due to the high thermal mass of the copper block. The heat transfer rate between the insulation and fluid accounts for less than 2 % of the total heat rate. Thus, nearly all heat transfer is between the copper block and the fluid.

4.4.3. Wall temperature distribution and dry-out areas

The wall temperature distribution forms a cool cross over the domain, as shown in Fig. 8 (a). The cross corresponds with the high liquid velocity distribution depicted in Fig. 8 (b). A large temperature gradient is formed from the base to the top of the fins in the cross-region, with a temperature difference of about 4 °C. The vapour column formed in Fig. 8 (b) heats the fins in the outer regions of the domain, decreasing the thermal gradient. A clear separation is shown in Fig. 8 between the liquid and vapour distributions, creating an upwash of vapour at the liquid–vapour interface. The cyclic behaviour of the dry-out and fully-developed nucleation boiling area contributions remain constant throughout the boiling curve, as displayed in Fig. 9. However, the cyclic behaviour only takes place if the fully developed nucleation boiling area contribution exceeds 20 %. The dry-out contribution has a local minimum of 0 % up until a heat flux of $27 W/cm^2$, as the liquid is not able to fully rewet a portion of the base area. The fully developed nucleate boiling area contribution increases with an increase in heat flux due to the fluid in the high liquid velocity regions entering the fully developed nucleate boiling region. The cyclic behaviour of the evaporation area contributions corresponds to the evaporation and condensation of a vapour column defined as an *iso*-surface where the cell vapour contribution > 0.5 in the pool boiling area, as shown in Fig. 10, for a constant input heat flux of $23.24 W/cm^2$. The cyclic behaviour of the dry-out area contribution can be linked to the see-saw behaviour of evaporation and quenching on the base wall. The high liquid-velocity region and cyclic behaviour of the vapour column represent the three main modes of heat transfer of the RPI wall-boiling model (convection, evaporation and condensation).It is important to note that Ansys Fluent's Eulerian multiphase model does not resolve the interface between the phases [32]. Vapour initiates at the base of the pin-fins, forming a blanket over the fins wherefrom it condenses into the bulk liquid. The vapour blanket phenomenon is also found by Bi *et al.* [36] in nanofluid boiling. They found that bubbles coalesce when they are too close to each other, resulting in a large vapour blanket covering the surface. Devahdhanush and Mudawar [2] and Cui *et al.* [7] implemented an array of jets to target the vapour columns formed at the outer regions of the domain.

5. Wall heat flux contributions

The convective heat flux is a maximum as the liquid accelerates just after the stagnation region, as shown in Fig. 11 (a). These regions of acceleration are also the regions with the highest liquid velocity shown in Fig. 8 (b) and Fig. 10 (blue *iso*-surfaces). The quenching contribution plot, shown in Fig. 11 (b), correlates to the flow boiling areas (outlined in Fig. 1 (b)) where the liquid can rewet the surface. The jet stagnation region is dominated by quenching as the impinging liquid continuously removes vapour formed under the jet. Finally, the highest evaporation contribution areas correspond, as shown in Fig. 11 (c), to the pool boiling areas and pin-fin wakes (outlined in Fig. 1 (b)) where quenching is minimal as the liquid cannot actively rewet the surface and evaporation dominates. The effect of pin-fin wake interference on the local boiling type is not investigated in this paper but is recommended for future researchers. The total heat flux, i.e. the sum of the previous three contributions as per the RPI model is plotted in Fig. 12. Comparison with Fig. 10 shows that the total flux is dominated by the evaporation heat flux (plotted in Fig. 11 (c)). The heat flux contribution plots in Fig. 11 and Fig. 12 are snapshots of the cycle illustrated in Fig. 10. Thus, the evaporation heat flux contribution will adhere to the vapour formation in Fig. 10.

5.0.1. Vapour fraction and turbulent kinetic energy

A linear increase in the volume-averaged turbulent kinetic energy is found throughout the boiling curve. This increase is due to the increased turbulent interaction between the liquid and the vapour as boiling increases over the surface. Slicing the domain between the stagnation region and outer edge defines a 45° diagonal plane. Contours on this plane are shown in Fig. 13 in the form of vapour faction and volume-averaged turbulent kinetic energy. The maximum vapour fraction (left) is located inside the core of the vapour column, dissipating to the outer regions of the vapour column. The rear ends of the outer pin-fins act as the origin of the large vapour column, coalescing with vapour formed at the front end of the outer pin-fins to create the large vapour
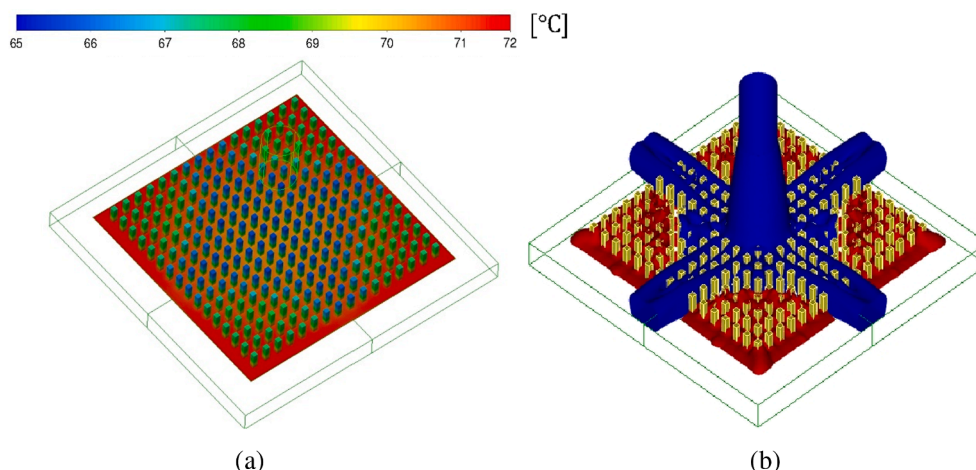

Fig. 8. Experimental validation: (a) wall temperature and (b) liquid velocity above 0.3 m/s (blue) and vapour fraction above 0.5 (red).
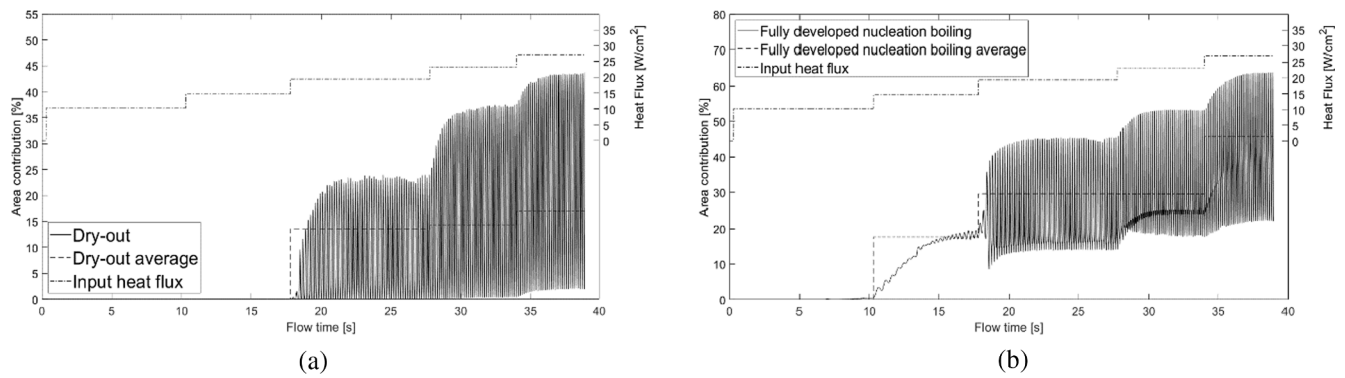
Fig. 9. Base surface evaporation area contribution with time of (a) dry-out area contribution and (b) fully developed nucleation boiling area contribution.
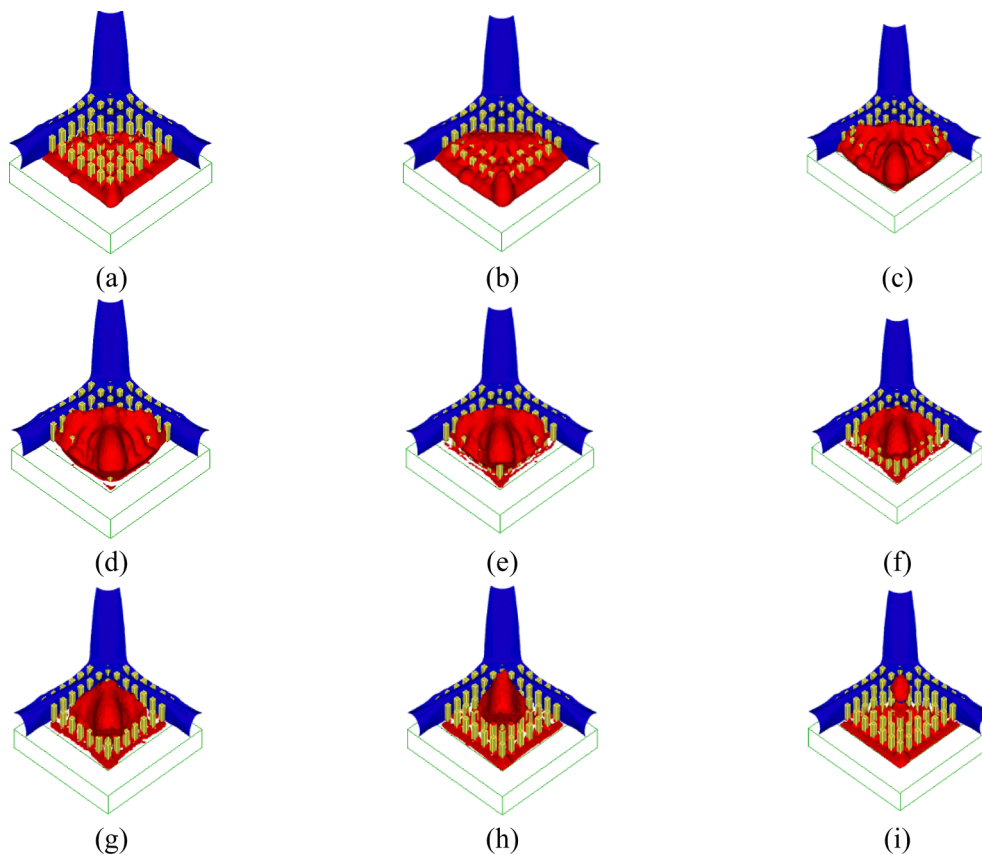

Fig. 10. Domain distribution of the liquid velocity above 0.3 m/s (blue) and cell vapour fraction above 0.5 (red) between frames (a) to (i), time series separated by intervals of 15 ms.

column. Fig. 13 also includes the time stamps relative to the initial plot with a frequency of the oscillation estimated to be 7.7 Hz. A maximum turbulent kinetic energy (scaled from 0 to 1) (right) is located just outside of the stagnation region as the liquid enters the staggered facing pin-fins. The local maximum in turbulent kinetic energy follows the vapour column as it grows and condenses. The local maximum of the vapour fraction does not correspond to the local maximum of the turbulent kinetic energy as the turbulent energy of vapour is much lower than that of the liquid phase.

6. Parametric studies

In this section, we investigate the effect of inlet Reynolds number, fin height and fin spacing on the heat transfer coefficient, pressure drop, and evaporation boiling area contributions. All results are time-

averaged after each simulation reaches a quasi-steady state. The parametric analysis considers the validation case in section 4 as the reference point when varying parameters.

6.1. Inlet Reynolds number

The inlet jet Reynolds number is lowered to 25 000 and raised to 45 000 as the base case has an inlet Reynolds number of 35 000. The inlet Reynolds numbers 25 000; 35 000, and 45 000 correspond to an inlet velocity of 1.94 m/s, 2.72 m/s, and 3.49 m/s, respectively. An apparent decrease in the stagnation wall superheat was obtained with a high jet Reynolds number (see Table 5). The increase in jet velocity leads to a higher stagnation pressure, increasing the hydrostatic pressure force exerted on evaporating bubbles in the stagnation regions. An increase in stagnation pressure also leads to a higher pressure drop between the
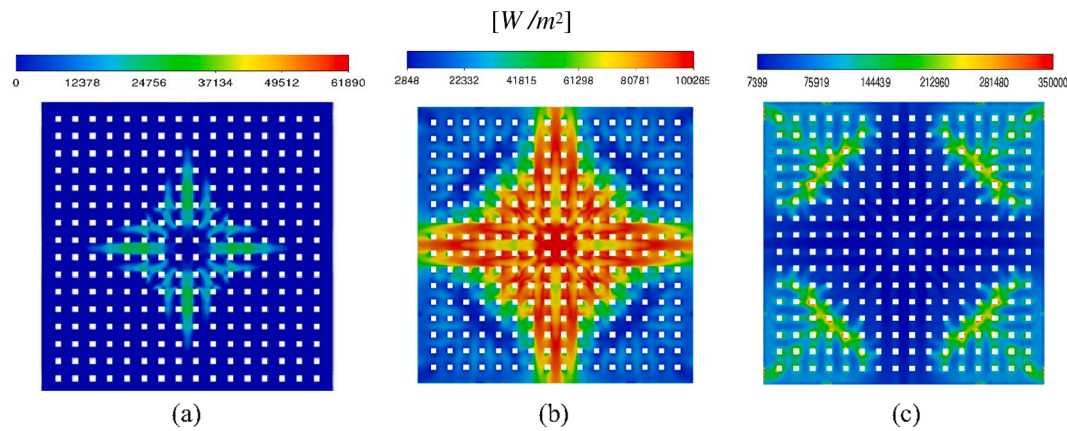
Fig. 11. Heat flux [W/cm^2] contributions plots at 23.24 W/cm^2 of (a) convective heat flux, (b) quenching heat flux and (c) evaporative heat flux.
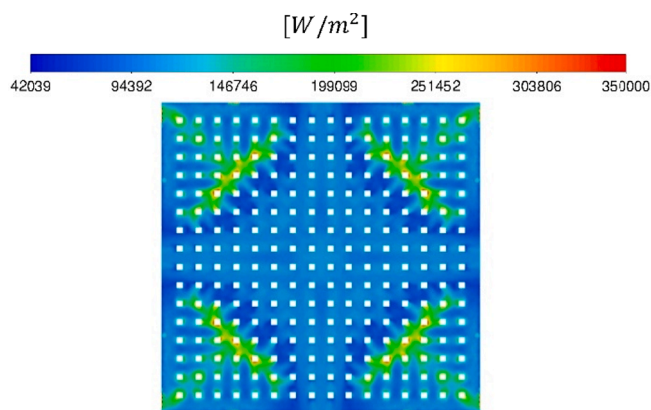

Fig. 12. Total heat flux contribution plot at 23.24 $\frac{W}{cm^2}$.

stagnation region and outlet boundaries, increasing the liquid acceleration towards the outlet and ultimately increasing heat transfer in the flow boiling regions. An increase in Reynolds number led to an approximate quadratic increase in pressure drop, as expected. The volume average turbulent kinetic energy remains approximately constant between the Reynolds numbers of 25 000 and 35 000. However, the volume of average turbulent kinetic energy is doubled at the high Reynolds number of 45 000. The increase in turbulent kinetic energy at the high Reynolds number results from the increased pressure difference between the stagnation region and the outlet boundary, increasing turbulence generated from the pin-fins as the fluid is forced towards the outlet boundary.

Fig. 14 illustrates the area contribution on the flat wall between the fins of each boiling type. An increase in the Reynolds number led to a slight decrease in the dry-out area contribution, reaching a plateau as the Reynolds number increased. Thus, it highlights that the Reynolds number has a limited influence on the dry-out region. Other parameters, such as fin height and pitch, need to be investigated to reduce the dry-out area contribution. The fully developed nucleate boiling regime contribution reached a minimum at the base case Reynolds number, with the developing nucleate boiling regime reaching a peak. The influence of Reynolds number on the fully developed and developing nucleate boiling area contributions is a complex phenomenon. The low liquid velocity in the flow boiling region at a Reynolds number of 25 000 struggles to actively remove forming bubbles from the heated surface. Thus, leading to a higher fully developed nucleate boiling region and a lower developing nucleate boiling region. An increase in Reynolds number increased the liquid velocity in the flow boiling regions, increasing the liquid ability to actively remove vapour from the

heated surface. Thus, increasing the developing nucleate boiling area contribution and decreasing the fully developed nucleate boiling area contribution. The slight increase in the fully developed nucleate boiling area contribution at the Reynolds number of 45 000 is due to the ability of the liquid to flow further into the staggered facing pin-fins before boiling.

6.2. Fin height and spacing

In this section, we investigate the effect of pin-fin height and spacing on the stagnation and average wall superheat on the base surface between the pin-fins. The investigation also includes the effect on pressure drop, volume averaged turbulent kinetic energy between the fins, nucleate boiling area contribution, and dry-out area contribution. Rau and Garimella [1] highlighted the importance of fin spacing when designing a pin-finned surface. This investigation aims to decrease the dry-out area contribution by increasing the fins spacing to allow for better liquid flow between the channels of the pin-fins and decreasing the pin-fin height to reduce flow obstruction caused by the fins, allowing the liquid to access the dry-out area.

All cases in this study are done at the same inlet jet Reynolds number of 35 000 and heat flux of 23.24 W/cm^2. The number of pin-fins in the domain is kept constant at 256. The surface augmentation factor, defined as the ratio between the total heat transfer area between a flat surface and the pin-fin surface, is constant throughout each spacing at a selected pin-fin height. The surface augmentation factor in Table 6 approximately halves between the highest and lowest fin height. The decrease in the augmentation factor may influence the heat transfer ability of the surface as the total area in which heat transfer occurs decreases.

An apparent increase in stagnation wall superheat (see Fig. 15 (a)) resulted from a decrease in fin height. As stated above, the decrease in the surface augmentation factor will harm heat transfer as the surface area of which heat can be transferred from the solid to the fluid decreases, thus, increasing the wall superheat. In addition, the increase in fin spacing led to a slight increase in stagnation wall.
superheat. The widening of flow channels will decrease flow obstruction from the stagnation region to the outlet, thereby decreasing the turbulence around the stagnation region and ultimately decreasing heat transfer.

A similar trend is gained from the average wall superheat of the flat surface between the pin-fins (see Fig. 15 (b)), with an increase in the average wall superheat resulting from a decrease in fin height. Again, this increase in wall superheat is due to the decrease in surface area. The highest average wall superheat is obtained at a fin spacing of 1.075 mm accros all fin heights. The pressure drop across all fin heights and spacings remain approximately constant (not shown). This confirms that the pressure drop across the domain is mainly driven by the dynamic
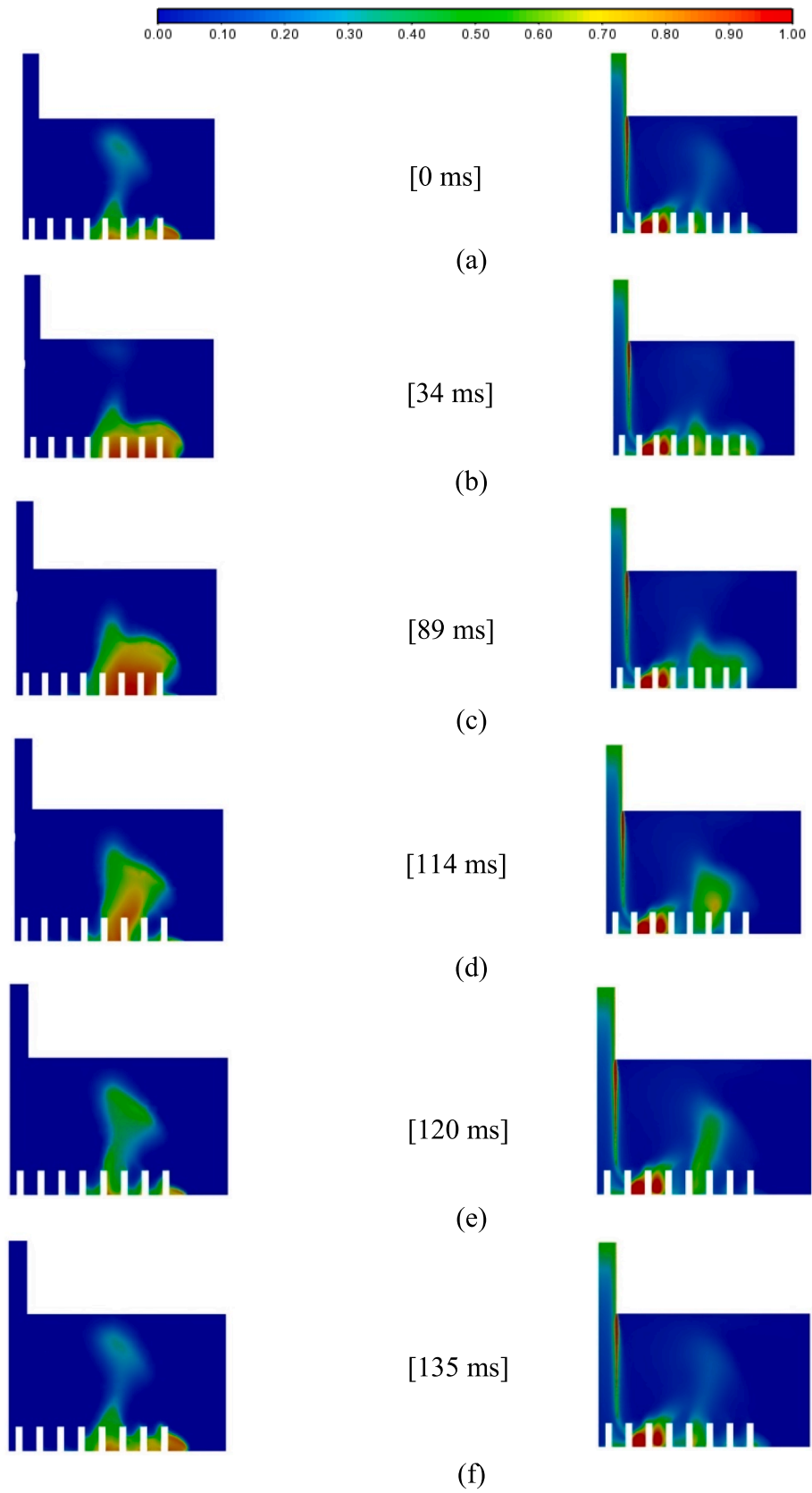
Fig. 13. 45°-plane 2D vapour fraction (left) and turbulent kinetic energy (right) cyclic behaviour.

Table 5
Parametric study: Inlet Reynolds number.

Inlet Reynolds number	Stagnation wall superheat [°C]	Maximum wall superheat [°C]	Pressure drop [ΔkPa]	Turbulent kinetic energy [m^2/s^2]
25 000	10.3	11.5	2.7	1.31e-02
35 000	9.8	11.0	5.5	1.26e-02
45 000	9.3	11.2	9.2	2.47e-02

pressure difference of the stagnating jet and not the flow obstruction caused by the pin-fins.

The average turbulent kinetic energy increases with a decrease in fin height, as depicted in Fig. 16. This increase in turbulent kinetic energy is due to the elimination of stagnation regions in the pin-fin region. As a result, the flow can move across the domain from the stagnation region, increasing the overall turbulence in the domain. Across all pin-fin heights, a local minimum is formed at a fin spacing of 1.075 *mm*. Compared to Fig. 15, a local maximum in average wall superheat resulted at a fin spacing of 1.075 *mm*, concluding that the average wall superheat increased at a fin spacing of 1.075 *mm* due to the reduction in turbulent kinetic energy at a fin spacing of 1.075 *mm*.
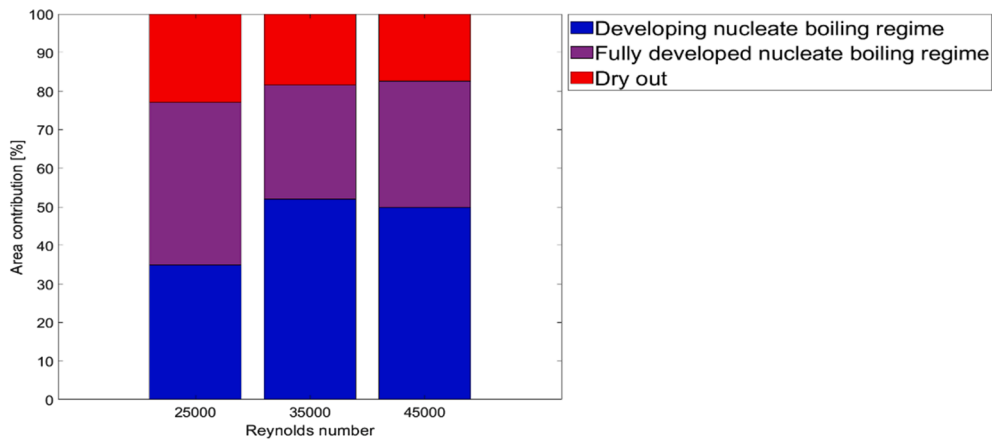
Fig. 17 (a) shows that dry-out is eliminated at a fin height of 0.312 *mm* and reached a peak at a fin height of 1.250 *mm* at spacings of 1.075 *mm* and 1.150 *mm*. The elimination of dry-out is linked to the volume-averaged turbulent kinetic energy in Fig. 16, as the highest turbulent kinetic energy eliminated dry-out. Turbulence enhanced the ability of the liquid to remove vapour from the heated surface, avoiding any damage to the heated surface. The dry-out area contribution at a fin height of 2.500 *mm* reduced from 16.7 % to 7.4 % when the fin spacing was increased whilst forming a small peak at a fin spacing of 1.075 *mm*. A similar trend resulted from all other fin heights.

Fig. 17 (b) shows the averaged fully developed nucleation boiling area contribution of the flat wall between the fins. An opposite trend resulted compared to the dry-out area contribution. A decrease in the dry-out area contribution led to the compromised areas entering the fully developed nucleate boiling regime, thus, increasing the area contribution.

If the pin-fin height is set at 1.25 *mm*, as shown in Fig. 18, the high liquid velocity region starts to engulf the vapour column, forming a cyclic wave as the evaporating vapour pushes the liquid upwards from the outer edge of the domain. For the lowest pin-fin height of 0.312 *mm*, shown in Fig. 19, the high liquid velocity region is able to cover the low

Fig. 14. Parametric study: Inlet Reynolds number boiling type area contribution.

Table 6
Parametric study: Fin height and spacing augmentation factor.

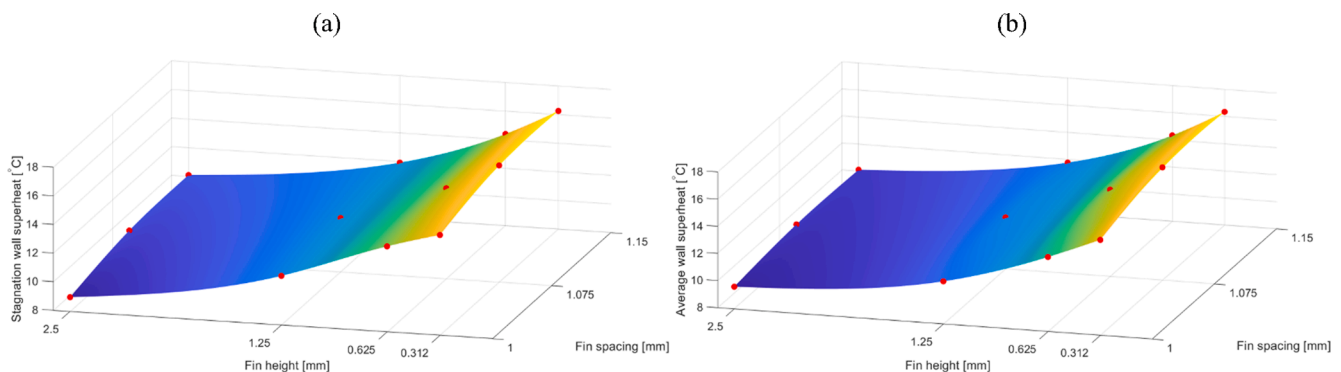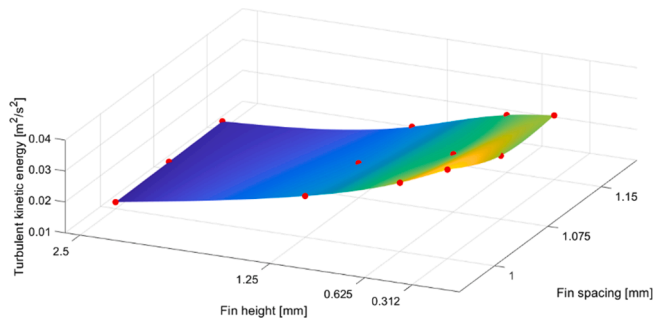| Fin height [*mm*]	Fin spacing [*mm*]		
	1.000	1.075	1.150
2.500	2.98	2.98	2.98
1.250	1.99	1.99	1.99
0.625	1.5	1.5	1.5
0.312	1.25	1.25	1.25

(a)　　　　　　　　　　　　　　　　　　　　(b)

Fig. 15. Parametric study: Fin height and spacing (a) stagnation wall superheat and (b) average wall superheat of the base surface between the pin-fins.

pin-fins, keeping the vapour column underneath the high liquid velocity region. For this case, the liquid flow over the pin-fins restricts the cyclic behaviour of the vapour column and the vapour column remains constant in its flat shape between the pin-fins.

6.3. Pin-fin distribution pattern

In this section, the effect of the pin-fin distribution pattern on heat transfer enhancement and dry-out region elimination is investigated. A star layout will potentially allow the liquid to reach the outer edges of the domain, decreasing the possibility of dry-out. The surface augmentation factor is decreased slightly from 2.98 to 2.92 to allow for a symmetric star arrangement. The star arrangement is inspired by Jenkins *et al.* [25] and consists of a flat surface at the jet stagnation region to allow the jet to spread towards the outer boundaries. The first ring of pin
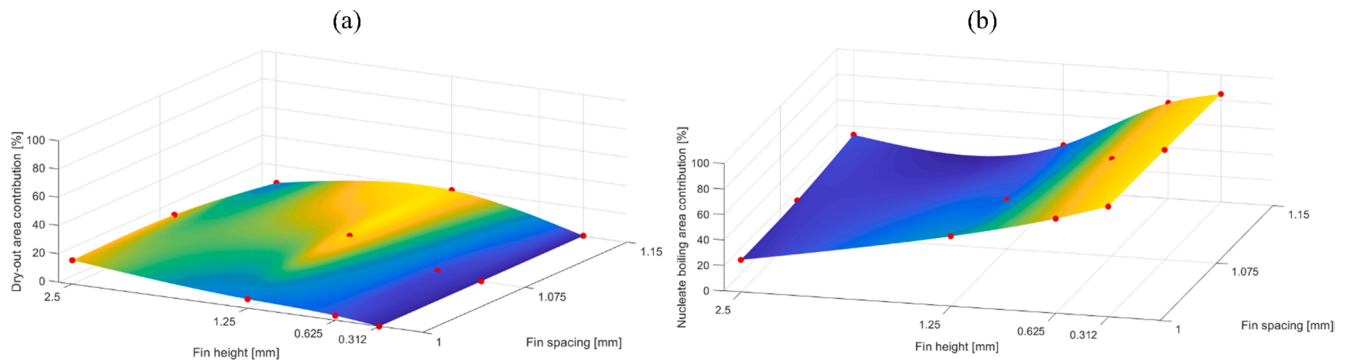

Fig. 16. Parametric study: Fin height and spacing volume averaged turbulent kinetic energy in the pin-fin region.

Fig. 17. Parametric study: Fin height and spacing (a) dry-out area contribution and (b) fully developed nucleate boiling area contribution.
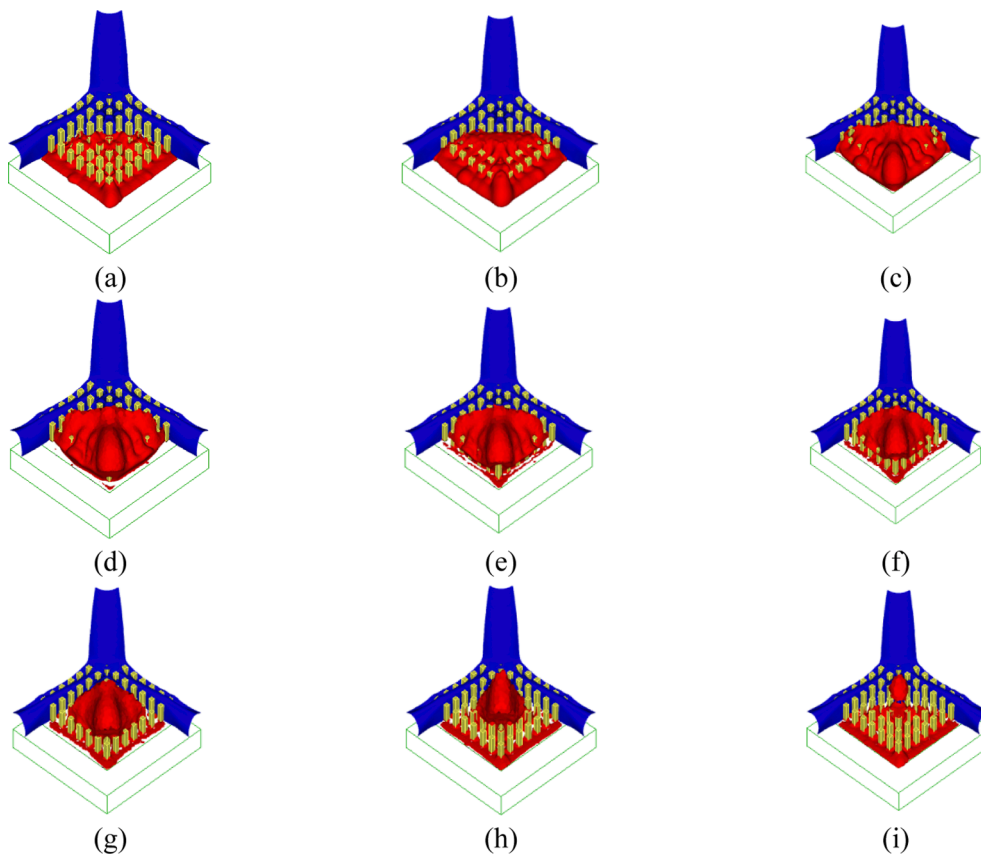

Fig. 18. Parametric study: Cyclic behaviour of a vapour column at a pin-fin height of 1.25 mm and spacing of 1.075 mm (liquid velocity above 0.3 m/s (blue) and cell vapour fraction above 0.5 (red) between frames (a) to (i)). Time series has intervals of 2 ms.
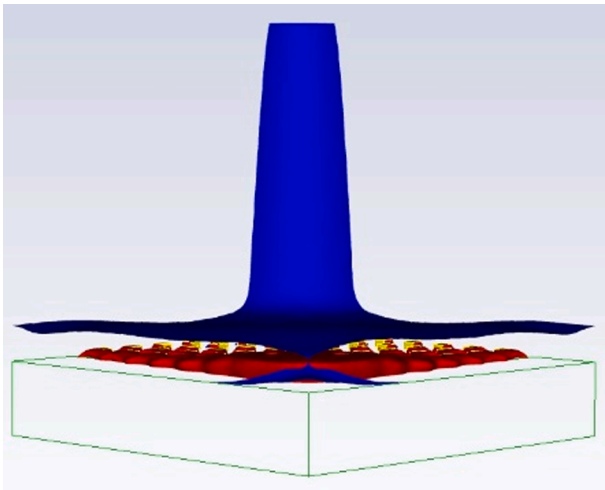
Fig. 19. Parametric study: Vapour column formation at a pin-fin height of 0.312 mm and spacing of 1.075 mm (liquid velocity above 0.3 m/s (blue) and cell vapour fraction above 0.5 (red)).

Fig. 21. Parametric study: Average base wall temperature boiling curve comparison between inline pin-fins and star pin-fins arrangement.

fins is placed at a diameter of 7.66 mm, and the successive rings of pin fins are placed at a radial pitch of 1.35 mm. The minimum distance between the pin fins in the first ring is 0.9 mm, wherefrom the spacing increases. An additional ray is created when the spacing between rows exceeds 2.3 mm, to increase the surface augmentation at the outer edges. The current study has the same liquid inlet velocity of 2.716 m/s and a constant input heat flux of $23.24 W/cm^2$ as the base case. A clear increase in high-velocity zones is obtained in the star arrangement compared to the inline arrangement, as shown in Fig. 20. Even though the pin-fin arrangement has changed at the stagnation region, the maximum liquid velocity at which the liquid accelerates after the stagnation region to the outlet boundary remains constant. As a result, the pressure drop across the domain for the two cases remained constant, highlighting the results from section 5.1, that the pressure drop is mainly driven by the velocity inlet stagnation and not the flow obstructions in the pin-fin regions.

The star arrangement led to a slight decrease in the average base wall superheat at an input heat flux of $23.24 W/cm^2$, even though the star arrangement has a slightly lower surface augmentation factor. The average dry-out area contribution at the base of the pin-fins decreases from 17 % to less than 1 %, eliminating the dry-out area contribution. In addition, the CHF of the star arrangement increases by a large amount, with the highest numerical result obtained having a dry-out area contribution of 40 % (see Fig. 20), located at the densely packed outer
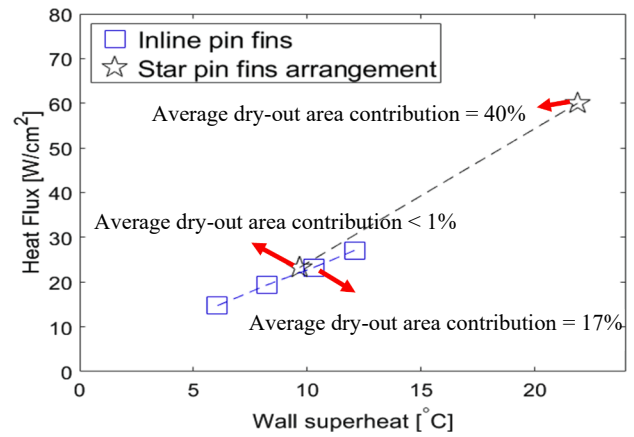
pin-fin region. The star arrangement led to a slight decrease in the average base wall superheat (see Fig. 21) at an input heat flux of $23.24 W/cm^2$ even though the star arrangement has a slightly lower surface augmentation factor. At this heat flux, the average dry-out area contribution at the base of the pin-fins decreases from 17 % to less than 1 %, eliminating the dry-out area contribution.

Fig. 22 depicts the heat flux contribution plot for the star pattern. The convective heat flux contribution (Fig. 22 (a)) increases with the star arrangement compared to the inline pin-fin arrangement, with a maximum contribution from outside the stagnation region as the liquid accelerates to the outer edges of the domain. The quenching heat flux (Fig. 22 (b)) is the dominant heat flux throughout the domain due to the liquid's ability to actively remove vapour from the heated surface due to decreased flow obstructions. Finally, the maximum evaporative heat flux (Fig. 22 (c)) is located at the outer edges of the domain as the density of the pin-fins increases. Therefore, the total heat flux (Fig. 22 (d)) is driven by the quenching heat flux, and is only expected to be dominated by the evaporative heat flux as for the in-line pattern at a higher heat fluxes.

Finally, Fig. 23 depicts the high liquid velocity and maximum vapour column distribution of the star pin-fin arrangement at the highest heat flux of $60 W/cm^2$. The high liquid velocity regions are now obstructed by the evaporation vapour column and not by pin-fins as was the case in Fig. 18, where the liquid formed a wave over the vapour column. The regions that contain a high density of vapour bubbles overlap with the high liquid-velocity regions due to the star arrangement of pin fins allowing the liquid to spread over the domain, contradicting the
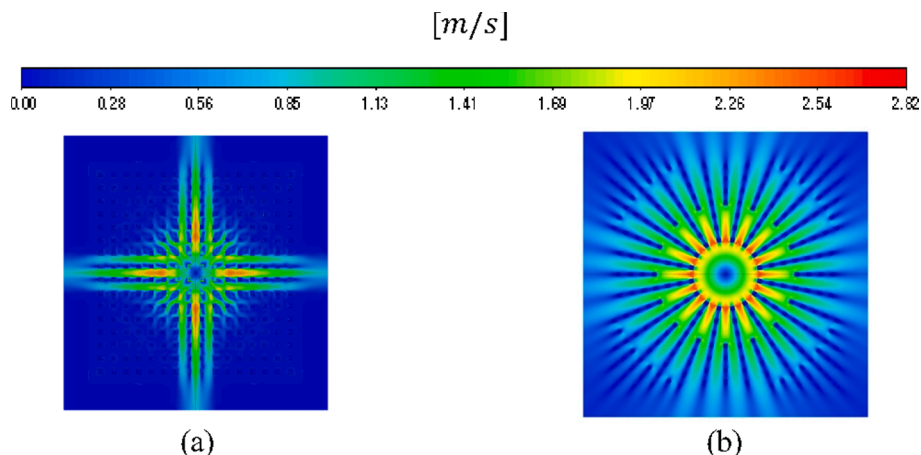
$[m/s]$

Fig. 20. Parametric study: Fin distribution liquid velocity of (a) inline arrangement and (b) star arrangement [m/s].
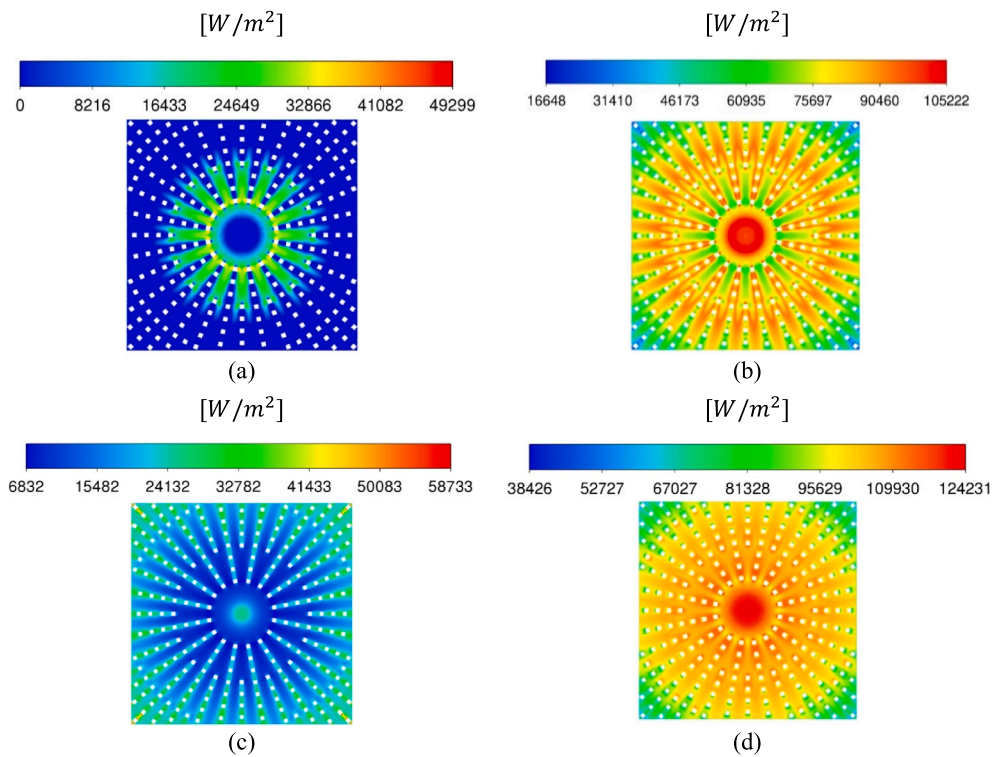
Fig. 22. Contour plots of the (a) liquid convective heat flux, (b) quenching heat flux, (c) evaporative heat flux and (d) the total heat flux at a star pin-fin distribution whilst kept at a constant heat flux of 23.24 W/cm^2.
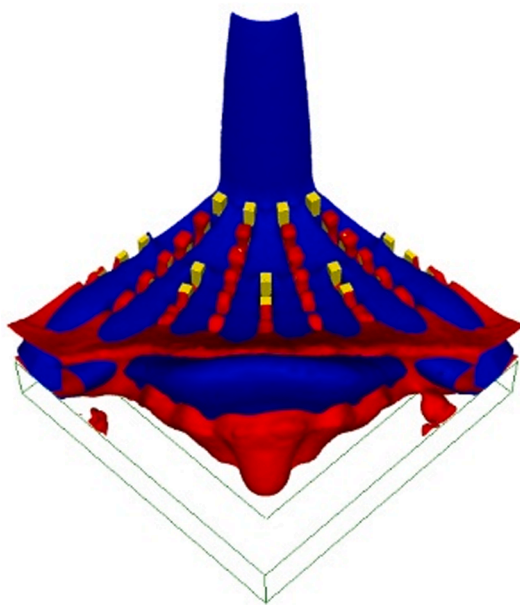

Fig. 23. Parametric study: star pin-fin arrangement liquid and vapour distribution at an input heat flux of $60 W/cm^2$ (liquid velocity above 0.3 m/s (blue) and cell vapour fraction above 0.5 (red)).

observations made with the in-line pin-fin arrangement.

This parametric study highlights the significant influence of pin-fin geometry and distribution on heat transfer performance. Nevertheless, it is crucial to acknowledge that several other techniques can be employed to further enhance heat transfer and mitigate the issue of local dry-out, as discussed in Section 1. In particular, the incorporation of nanoparticles in the working fluid can be a viable approach to further augment surface wettability, reduce the rate and diameter of bubble

departure, and thereby alleviate the occurrence of local dry-out regions as identified in this study.

7. Conclusion

This study presents the computational validation and optimisation of boiling jet impingement heat transfer on pin-fin surfaces. The key aspects of the study are:

(1) The inclusion of structured surfaces in boiling jet impingement results in highly complex flow patterns, creating different boiling regimes throughout the domain, including convection and quenching at the jet stagnation region, flow boiling in the pin-fin -formed channels perpendicular to the stagnation region and pool boiling in the outer regions of the domain due to the flow obstruction caused by the pin-fins.
(2) The validation against experimental results gave confidence that the model can successfully predict heat transfer.
(3) A parametric study presenting the influence of jet inlet Reynolds number, pin-fin height, spacing and distribution was then conducted.

The key findings from this study are:

(1) The inclusion of a y^+ insensitive near-wall treatment model increases numerical stability and accuracy due to the complex flow patterns between the pin-fins. When increasing the mesh density in the pin-fin vicinity, the accuracy of the numerical model was increased with hexahedral and polyhedral cells predicting identical stagnation wall temperatures with eight cells between opposing pin-fins. Hexahedral cells are the preferred cell type as they decrease computational costs whilst keeping the same accuracy level.

(2) The Rensselaer Polytechnic Institute boiling model successfully predicted heat transfer up until the pool boiling regions reached dry-out whereafter numerical instabilities arose.

(3) The fully developed nucleation boiling and dry-out area contributions displayed cyclic behaviour over time due to the formation and dissipation of vapour in the outer regions of the domain.

(4) The temperature distribution on the top wall formed a cross through the domain, agreeing with the high liquid velocity distribution. The liquid temperature at the outer edges of the domain created hot pockets around the vapour columns as the liquid transitioned to a vapour.

(5) The distribution of liquid velocity across the domain is not affected by inlet jet velocity but by flow obstruction caused by the distribution and dimensions on the pin fins, limiting the ability to reduce dry-out areas.

(6) The decrease in pin-fin height and increase in pin-fin spacing both reduce flow obstruction and allow liquid to reach the outer edges of the domain, reducing the dry-out area contributions.

(7) The decrease in the surface augmentation factor is detrimental to heat transfer as it decreases the surface area of which heat can be transferred from the solid to the fluid.

(8) Increasing high-velocity regions through decreasing flow obstruction eliminates the possibility of dry-out. This concept is showcased in the star pin-fin arrangement where high liquid-velocity regions are increased and pool boiling areas are practically eliminated. It is highly recommended that future researchers consider optimising liquid spreading throughout the domain to enhance heat transfer and decrease local dry-out.

(9) Heat transfer remains constant with different pin-fin configurations at the same surface augmentation factor. Therefore, it is concluded that heat transfer is mainly linked to surface augmentation.

CRediT authorship contribution statement

L. Ludick: Conceptualization, Methodology, Validation, Visualization, Writing – original draft. **K.J. Craig:** Conceptualization, Writing – review & editing. **P. Valluri:** Conceptualization, Writing – review & editing, Funding acquisition. **J.P. Meyer:** Writing – review & editing.

Declaration of Competing Interest

The authors declare that they have no known competing financial interests or personal relationships that could have appeared to influence the work reported in this paper.

Data availability

Data will be made available on request.

Acknowledgements

Appendix A. Numerical framework

The Eulerian approach is a method to develop equations for a collection of fluid elements at a fixed region in space [35], and multiphase flows are treated as interpenetrating continua where volume fractions represent the space of each phase occupied in a control volume and expressed as.

$$V_q = \int \alpha_q dV \tag{A-1}$$

where the sum of the volume fractions (α_q) at each phase is equal to 1 inside of a control volume. The effective density of each phase is expressed as

$$\widehat{\rho}_q = \alpha_q \rho_q \tag{A-2}$$

and ρ_q is the physical density of the phase q. Eq(A-2). can be implicitly solved through

$$\frac{\alpha_q^{n+1}\rho_q^{n+1} - \alpha_q^n\rho_q^n}{\Delta t}V + \sum_f \left(\rho_q^{n+1}U_f^{n+1}\alpha_{q,f}^{n+1}\right) = \left[S_{\alpha q} + \sum_{p=1}^n \left(\dot{m}_{pq} - \dot{m}_{qp}\right)\right]V \tag{A-3}$$

where n denotes the current time step, and n + 1 is the next time step. α_q denotes the volume fraction cell value, $\alpha_{q,f}$ the face value of the qth volume fraction and V the cell volume. $\dot{m}_{pq}$ represents the mass transfer from phase p to phase q and $\dot{m}_{qp}$ the mass transfer from phase q to phase p. The mass source term $S_{\alpha q}$ is usually set to zero. Each phase's mass, momentum and energy conservation laws are met individually. The derivation is done by ensembling the average local instantaneous balance for each phase, where each phase is coupled through pressure and interphase interaction coefficients [37].

Conservation equations

The continuity equation for phase q is expressed as.

$$\frac{\partial}{\partial t}\left(\alpha_q \rho_q\right) + \nabla \bullet \left(\alpha_q \rho_q \overrightarrow{v}_q\right) = \sum_{p=1}^n \left(\dot{m}_{pq}\right) + S_q \tag{A-4}$$

where $\overrightarrow{v}_q$ is the velocity of phase q, and again the source term S_q is usually set to zero. If there is no phase change present, $\dot{m}_{pq}$ drops out of Eq(A-4). The momentum equation is expressed as

$$\frac{\partial}{\partial t}\left(\alpha_q\rho_q\overrightarrow{v}_q\right)+\nabla\bullet\left(\alpha_q\rho_q\overrightarrow{v}_q\overrightarrow{v}_q\right) = -\alpha_q\nabla p+\nabla\bullet\overline{\overline{\tau}}_p+\alpha_q\rho_q\overrightarrow{g}+\sum_{p=1}^{n}\left(\overrightarrow{R}_{pq}+\dot{m}_{pq}\overrightarrow{v}_{pq}\right)+F \tag{A-5}$$

where ∇p is the shared pressure across all phases, $\overline{\overline{\tau}}_p$ is the stress tensor, $\overrightarrow{R}_{pq}$ an interaction force between phases p and q, n the number of phases, $\overrightarrow{v}_{pq}$ the interphase velocity and

$$F = \left(\overrightarrow{F}_q+\overrightarrow{F}_{lift,q}+\overrightarrow{F}_{wl,q}+\overrightarrow{F}_{vm,q}+\overrightarrow{F}_{td,q}\right) \tag{A-6}$$

where $\overrightarrow{F}_q$ the external body force, $\overrightarrow{F}_{lift,q}$ the lift force, $\overrightarrow{F}_{wl,q}$ the wall lubrication force, $\overrightarrow{F}_{vm,q}$ the virtual mass force and $\overrightarrow{F}_{td,q}$ is the turbulent dispersion force in the case of turbulent flow. $\overline{\tau}$ defines the q phase stress–strain tensor expressed as

$$\overline{\overline{\tau}}_q = \alpha_q\mu_q\left(\nabla\overrightarrow{v}_q+\nabla\overrightarrow{v}_q^T\right)+\alpha_q\left(\lambda_q-\frac{2}{3}\mu_q\right)\nabla\overrightarrow{v}_q\overline{I} \tag{A-7}$$

The interaction force between phases is expressed as.

$$\sum_{p=1}^{n}\overrightarrow{R}_{pq} = \sum_{p=1}^{n}K_{pq}\left(\overrightarrow{v}_p-\overrightarrow{v}_q\right) \tag{A-8}$$

where K_{pq} in the interphase momentum exchange coefficient. The conservation of energy is described as a separate enthalpy equation of each phase and expressed as

$$\frac{\partial}{\partial t}\left(\alpha_q\rho_q h_q\right)+\nabla\bullet\left(\alpha_q\rho_q\overrightarrow{v}_q h_q\right) = \overline{\overline{\tau}}_q:\nabla\bullet\overrightarrow{v}_q-\nabla\bullet\overrightarrow{q}_q+\sum_{p=1}^{n}\left(Q_{pq}+\dot{m}_{pq}h_{pq}\right)+p\frac{\partial\alpha_q}{\partial t}+S_q \tag{A-9}$$

where h_q is the specific enthalphy of phase q, $\overrightarrow{q}_q$ is the heat flux, S_q the energy source term, $\overrightarrow{J_q}$ the diffusive heat flux in phase q, Q_{pq} the heat exchange intensity between phases p and q, and h_{pq} is the interphase enthalpy.

Turbulence modelling

Multiphase turbulence is modelled through the renormalisation (RNG) $k-\varepsilon$ mixture turbulence model, where an additional source term is added to the turbulence dissipation equation to account for the dispersed phase-induced turbulence and the differences between the production and destruction thereof. The turbulent kinetic equation is expressed as.

$$\frac{\partial}{\partial t}\left(\rho_m k\right)+\nabla\bullet\left(\rho_m\overrightarrow{v}_m k\right) = -\nabla\bullet\left(\sigma_{k,m}\mu_{t,m}\nabla k\right)+G_{k,m}-\rho_m\varepsilon+S_{k_m} \tag{A-10}$$

where ρ_m is the mixture density, $\overrightarrow{v}_m$ is the mixture velocity, μ_m is the mixture of dynamic viscosity, k the turbulent kinetic energy, ε the turbulent dissipation rate, $\mu_{t,m}$ the mixture turbulent viscosity, $\sigma_{k,m}$ the inverse of the effective Prandtl number for k, $G_{k,m}$ the production of turbulent kinetic energy and S_{k_m} the source term to include the dispersed phase-induced turbulence for k. The turbulent dissipation rate is expressed as

$$\frac{\partial}{\partial t}\left(\rho_m\varepsilon\right)+\nabla\bullet\left(\rho_m\overrightarrow{v}_m\varepsilon\right) = -\nabla\bullet\left(\sigma_{\varepsilon,m}\mu_{t,m}\nabla\varepsilon\right)+\frac{\varepsilon}{k}\left(C_{1\varepsilon}G_{k,m}-C_{2\varepsilon}\rho_m\varepsilon\right)+S_{\varepsilon_m}-R_\varepsilon$$

where $\sigma_{\varepsilon,m}$ is the inverse of the effective Prandtl number for ε, $C_{1\varepsilon}$ and $C_{2\varepsilon}$ are model constants, S_{ε_m} the source term to include the dispersed phase-induced turbulence for ε and R_ε the RNG additional term. The factor $\frac{\varepsilon}{k}$ in Eq(A-11). ensures that the production and destruction of turbulent kinetic energy are always closely related and avoid non-physical negative values of the turbulent kinetic energy if k decreases [35]. The mixture properties discussed above are expressed as.

$$\rho_m = \sum_{i=1}^{N}\alpha_i\rho_i \tag{A-12}$$

$$\mu_m = \sum_{i=1}^{N}\alpha_i\mu_i \tag{A-13}$$

$$\overrightarrow{v}_m = \frac{\sum_{i=1}^{N}\alpha_i\rho_i\overrightarrow{v}_i}{\sum_{i=1}^{N}\alpha_i\rho_i} \tag{A-14}$$

where α_i is the phase volume fraction, ρ_i the phase density, μ_i the phase dynamic viscosity, and $\overrightarrow{v}_i$ the phase velocity. The mixture of turbulent viscosity is expressed as

$$\mu_{t,m} = \rho_m C_\mu\frac{k^2}{\varepsilon} \tag{A-15}$$

where C_μ is a model constant. The production of turbulent kinetic energy is expressed as

$$G_{k,m} = \mu_{t,m}\left(\nabla \vec{v}_m + \left(\nabla \vec{v}_m\right)^T\right) : \nabla \vec{v}_m \tag{A-16}$$

Near wall modelling is outlined in section 3.

Interphase transfer models.

The interfacial area concentration is an important parameter as a strong relationship exists between the transport terms of interfacial area concentration and mass, momentum and energy [37]. The interfacial area concentration can be defined through the Ishii model, which results in a piecewise linear function of α_p that approaches 0 if α_p approaches 1 that switches the model of if there is no boiling present in the domain and is expressed as.

$$A_i = \frac{6(1-\alpha_p)\min\left(\alpha_p, \alpha_{p,crit}\right)}{d_p\left(1 - \min\left(\alpha_p, \alpha_{p,crit}\right)\right)} \tag{A-17}$$

where α_p is the volume fraction of the liquid phase, d_p is the bubble diameter and $\alpha_{p,crit} = 0.25$. The evaporation–condensation model [32] determines the liquid–vapour mass transfer rates included in Eq(A-5). The summation of mass transfer from the wall to the vapour and interfacial mass transfer is expressed as [29]

$$\sum_{p=1}^{n}\left(\dot{m}_{pq}\right) = m_{lv} = \frac{[h_{ls}(T_l - T_{sat}) + h_{vs}(T_v - T_{sat})]A_i}{h_{fg}} + \frac{q_E^{''}A_{i,W}}{h_{fg} + C_{p,l}(T_s - T_l)} \tag{A-18}$$

where h_{ls} and h_{vs} is the liquid and vapour side interfacial heat transfer coefficient, respectively. h_{fg} is the latent heat of vaporisation, T_l and T_v the liquid and vapour temperature, $q_E^{''}$ the evaporative heat flux component of the RPI boiling model (discussed later), $A_{i,W}$ the interfacial area density of the wall, and $C_{p,l}$ the liquid heat capacity. h_{ls} and h_{vs} is related to the phase Nusselt number by

$$h_{pq} = \frac{\kappa_q Nu_p}{d_p} \tag{A-19}$$

The Tomiyama correlation [38] is used to express the Nusselt number as.

$$Nu_p = 2.0 + 0.15 Re_p^{0.8} Pr^{0.5} \tag{A-20}$$

The Tomiyama correlation is frequently used for bubbly flows with a relatively low Reynolds number [32]. The interphase momentum exchange expressed in Eq(A-8) is defined as.

$$K_{pq} = \frac{\rho_p f}{6\tau_p}d_p A_i \tag{A-21}$$

where τ_p is the particulate relaxation time and is expressed as

$$\tau_p = \frac{\rho_p d_p^2}{18\mu_q} \tag{A-22}$$

and f is the drag function and is expressed as

$$f = \frac{C_D Re}{24} \tag{A-23}$$

The Drag coefficient can be modelled through the Ishii model [37] in bubbly flow and is expressed as.

$$C_D = \min\left(\frac{24}{Re}\left(1 + 0.15 Re^{0.75}\right), \frac{2}{3}\frac{d_p}{\left(\frac{\sigma}{g|\rho_p - \rho_g|}\right)^{\frac{1}{2}}}\right) \tag{A-24}$$

where the drag is calculated based on the minimum between the viscous and distorted region, Re is the relative Reynolds number, g is gravity, and σ is the surface tension. The lift force in Eq(A-6) is expressed as

$$\vec{F}_{lift} = -C_l \rho_q \alpha_p \left(\vec{v}_q - \vec{v}_p\right) \times \left(\nabla \times \vec{v}_q\right) \tag{A-25}$$

where C_l is the lift coefficient and can be modelled through the Tomiyama Lift Force model [38], which is expressed as

$$C_l = \begin{cases} \min\left[0.228 tanh\left(0.121 Re_p\right), f(Eo')\right] if Eo' \le 4 \\ f(Eo') if 4 < Eo' \le 10 \\ -0.27 if Eo' \ge 10 \end{cases} \tag{A-26}$$

where

$$f(Eo') = 0.00105Eo'^3 - 0.0159Eo'^2 - 0.0204Eo' + 0.474 \tag{A-27}$$

where Eo' is defined as the modified Eötvös number and expressed as

$$Eo' = \frac{g(\rho_q - \rho_p)d_h^2}{\sigma} \tag{A-28}$$

where σ is the surface tension coefficient and its surface dependent, d_h is the long axis of the deformable bubble and expressed as

$$d_h = d_b(1 + 0.163Eo^{0.757})^{1/3} \tag{A-29}$$

and

$$Eo = \frac{g(\rho_q - \rho_p)d_b^2}{\sigma} \tag{A-30}$$

The wall lubrication force is expressed as.

$$\overrightarrow{F}_{wl} = C_{wl}\rho_q\alpha_p\left|\left(\overrightarrow{v}_q - \overrightarrow{v}_p\right)\right|^2 \overrightarrow{n}_w \tag{A-31}$$

where C_{wl} is the wall lubrication coefficient, $\left|\overrightarrow{v}_q - \overrightarrow{v}_p\right|$ is the phase relative velocity component tangential to the wall surface and $\overrightarrow{n}_w$ is the unit normal, pointing away from the wall. The Antal et al. model [39] can be used to model the wall lubrication coefficient and is expressed as

$$C_{wl} = \max\left(0, \frac{C_{w1}}{d_b} + \frac{C_{w2}}{y_w}\right) \tag{A-32}$$

where $C_{w1} = -0.01 and C_{w2} = 0.05$, y_w is the distance to the nearest wall. The turbulent dispersion force can be modelled by the Lopez de Bertodano model [40] and is expressed as

$$\overrightarrow{F}_{td,q} = -\overrightarrow{F}_{td,p} = -C_{TD}\rho_q k_q \nabla\alpha_p \tag{A-33}$$

where k_q is the turbulent kinetic energy, $\nabla\alpha_p$ is the gradient of the dispersed phase volume fraction and C_{TD} is a constant, which is usually 1. The virtual mass force occurs when the vapour phase accelerates relative to the liquid phase due to the significant difference in density between the liquid and vapour phase, and the inertia of the liquid phase mass is encountered by the accelerating particles, which exerts a force on the particles. This phenomenon is expressed as

$$\overrightarrow{F}_{vm} = C_{vm}\rho_q\alpha_p\left(\frac{d_q\overrightarrow{v}_q}{dt} - \frac{d_p\overrightarrow{v}_p}{dt}\right) \tag{A-34}$$

where C_{vm} is the virtual mass coefficient and is chosen to be the theoretical value of 0.5 for a spherical bubble in an infinite medium [30]. Turbulence interaction can be modelled through the Troshko-Hassam turbulence models [41], which accounts for the turbulence of the dispersed phase in the $k - \epsilon$ equations in Eq(A-10). and Eq(A-11). The interaction terms when using mixture turbulence models are

$$S_{k_m} = C_{ke}K_{pq}\left|\overrightarrow{v}_p - \overrightarrow{v}_q\right|^2 \tag{A-35}$$

and

$$S_{\varepsilon_m} = C_{td}\frac{1}{\tau_p}S_{km} \tag{A-36}$$

and the constants $C_{ke} = 0.75$ and $C_{td} = 0.45$. The characteristic time of the induced turbulence is expressed as

$$\tau_p = \frac{2C_{vm}d_p}{3C_D\left|\overrightarrow{v}_p - \overrightarrow{v}_q\right|} \tag{A-37}$$

Wall boiling model.
Kurul and Podowski [11] established the RPI wall boiling model, which explained that the total wall heat flux consists of three components and is expressed as.

$$\dot{q}_W = \dot{q}_C + \dot{q}_Q + \dot{q}_E \tag{A-38}$$

where $\dot{q}_C$ relates to the convective heat flux, $\dot{q}_Q$ to the quenching heat flux and $\dot{q}_E$ to the evaporative heat flux. The convective heat flux is expressed as

$$\dot{q}_C = h_c(T_w - T_l)(1 - A_b) \tag{A-39}$$

where h_c is the single-phase convective heat transfer, T_w the wall temperature, T_l the liquid temperature and A_b the effective area of influence refers to the area occupied by bubbles across the nucleation site [37]. Quenching heat flux is expressed as

$$\dot{q}_Q = C_{wt}\frac{2K_l(T_w - T_l)}{\sqrt{\pi\lambda_l T}} \tag{A-40}$$

where K_l is the liquid thermal conductivity, λ_l the liquid diffusivity and T the periodic time, which is cyclic averaged, T_l the near wall liquid temperature, and C_{wt} a Fluent introduced correcting time between consecutive bubbles, which is chosen as 1. This process refers to the average heat transfer due to the instant periodic displacement of cold liquid after removing bubbles from the impinged surface [37]. The evaporative heat flux is expressed as

$$\dot{q}_E = V_d N_w \rho_v f h_{fv} \tag{A-41}$$

where V_d is the volume of the bubble at its departure diameter, N_w is the nucleation site density, which is greatly influenced by microscale surface roughness, ρ_v the vapour density, f the bubble departure frequency and h_{fv} the latent heat for vaporisation [37]. The effective area is expressed as

$$A_b = \min\left(1, K\frac{N_w \pi D_w^2}{4}\right) \tag{A-42}$$

where D_w is the bubble departure diameter, and the empirical constant K is modified by Del Valle and Kenning [42] and expressed as

$$K = 4.8e^{(-0.0125Ja_{sub})} \tag{A-43}$$

where the subcooled Jacob number is expressed as

$$Ja_{sub} = \frac{\rho_l C_{pl} \Delta T_{sub}}{\rho_v h_{fg}} \tag{A-44}$$

The bubble departure frequency was calculated by Cole [43] through a photographic study of pool boiling of distilled water in the region just before the CHF and expressed as.

$$f = \frac{1}{T} = \sqrt{\frac{4g(\rho_l - \rho_v)}{3\rho_l D_w}} \tag{A-45}$$

Nucleation site density has a neglectable effect on both the liquid temperature and the gas volume fraction but has a large impact on the wall superheat [44] and is expressed as.

$$N_w = C^n(T_w - T_{sat})^n \tag{A-46}$$

where Lemmert and Chawla [45] suggested empirical coefficients of

$$n = 1.805 \& C = 210 \tag{A-47}$$

The evaporation heat flux is highly dependent on the prediction of the bubble departure diameters. The Unal [46] calculates the bubble departure diameter as.

$$D_w = 2.42 \times 10^{-5} p^{0.709}\left(\frac{a}{b\sqrt{\varphi}}\right) \tag{A-48}$$

where

$$a = \frac{T_w - T_{sat}}{2\rho_v h_{fg}}\sqrt{\frac{\rho_s C_{ps} k_s}{\pi}} \tag{A-49}$$

$$b = \begin{cases} \dfrac{\Delta T_{sub}}{2\left(1 - \dfrac{\rho_v}{\rho_l}\right)}e^{\left(\frac{\Delta T_{sub}}{3} - 1\right)} & for\, \Delta T_{sub} \leq 3 \\[2em] \dfrac{\Delta T_{sub}}{2\left(1 - \dfrac{\rho_v}{\rho_l}\right)} & for\, \Delta T_{sub} \geq 3 \end{cases} \tag{A-50}$$

$$\varphi = max\left(\left(\frac{U_b}{U_o}\right)^{0.47}, 1.0\right) \tag{A-51}$$

where U_b is the near-wall bulk velocity, $U_o = 0.61 m/s$, and subscripts $s, l, and v$ denote the solid material, liquid, and vapour phase, respectively. The

implementation of the Unal correlation considers local pressure, amount of subcooling and wall superheat. All equations and models in this section are already implemented in Ansys Fluent, and one assumes that all models are implemented correctly due to their policy.

References

[1] M.J. Rau, S.V. Garimella, Confined jet impingement with boiling on a variety of enhanced surfaces, Am. Soc. Mech. Eng. J. Heat Trans. 136 (2014).

[2] V.S. Devahdhanush, I. Mudawar, Review of critical heat Flux (CHF) in jet impingement boiling, Int. J. Heat Mass Transf. 169 (2021).

[3] Z. Zhang, X. Wang, Y. Yan, A review of the state-of-the-art in electronic cooling, e-Prime – Adv. Elect. Eng. Electron. Energy Convers. Manage. 1 (2021).

[4] C. Agrawal, Surface quenching by jet impingement, A review, Steel Res. Int. 90 (1800285) (2019).

[5] K.S. Choo, S.J. Kim, Comparison of thermal characteristics of confined and unconfined impinging jets, Int. J. Heat Mass Transf. 53 (2010) 3366–3371.

[6] R. Viskanta, Heat transfer to impinging isothermal gas and flame jets, Exp. Therm Fluid Sci. 6 (1993) 111–134.

[7] F.L. Cui, F.J. Hong, P. Cheng, Comparison of normal and distributed jet array impingement boiling of HFE-7000 on smooth and pin-fin surfaces, Int. J. Heat Mass Transf. 126 (2018) 1287–1298.

[8] V.S. Devahdhanush, I. Mudawar, Critical heat flux of confined round single jet and jet array impingement boiling, Int. J. Heat Mass Transf. 169 (2021).

[9] Y.K. Katto, M. Kunihiro, Study of the mechanism of burn-out in boiling system of high burn-out heat flux, The Japan Society of Mechanical Engineers, International Journal 16 (1973) 1357–1366.

[10] M.J. Rau, S.V. Garimella, Local two-phase heat transfer from arrays of confined and submerged impinging jets, Int. J. Heat Mass Transf. 67 (2013) 487–498.

[11] M.J. Rau, S.V. Garimella, E.M. Dede, S.N. Joshi, Boiling heat transfer from an array of round jets with hybrid surface enhancements, Am. Soc. Mech. Eng. J. Heat Transfer 137 (2015).

[12] X. Ji, X. Ma, X. Yang, J. Wei, B. Sundén, Jet array impingement boiling in compact space for high heat flux cooling, Appl. Therm. Eng. 219 (2023).

[13] I. Pranoto, M.A. Rahman, J. Waluyo, The role of pin fin array configurations and bubble characteristics on the pool boiling heat transfer enhancement, Fluids 7 (2022).

[14] Z. Cheng, X. Li, X. Huai, F. Dong, Boiling heat transfer characteristics of pin-finned surface in distributed jet array impingement, Int. J. Therm. Sci. 184 (2023).

[15] S. Feng, Y. Yan, C. Lai, Experimental study on flow boiling characteristics of hybrid micro-channels with gradient distribution pillars and bypass, Int. J. Heat Mass Transf. 186 (2022).

[16] D. Wen, Influence of nanoparticles on boiling heat transfer, Appl. Therm. Eng. 41 (2012) 2–9.

[17] Y. Song, X. Ma, Y. Wang, S. Yao, K. Vafai, Amelioration of boiling heat transfer by 3D deposition structure of graphene-silver hybrid nanoparticle, Energy Convers. Manage.: X 12 (2021).

[18] V.O. Ng, H. Yu, H.A. Wu, Y.M. Hung, Thermal performance enhancement and optimization of two-phase closed thermosyphon with graphene-nanoplatelets coatings, Energ. Conver. Manage. 236 (2021).

[19] A. Mehralizadeh, S.R. Shabanian, G. Bakeri, Effect of modified surfaces on bubble dynamics and pool boiling heat transfer enhancement: A review, Therm. Sci. Eng. Prog. 15 (2020).

[20] X. Ma, Y. Song, Y. Wang, Y. Zhang, J. Xu, S. Yao, K. Vafai, Experimental study of boiling heat transfer for a novel type of GNP-Fe$_3$O$_4$ hybrid nanofluids blended with different nanoparticles, Powder Technol. 396 (2022) 92–112.

[21] X. Ma, Y. Song, Y. Wang, S. Yao, K. Vafai, Amelioration of pool boiling thermal performance utilizing graphene-silver hybrid nanofluids, Powder Technol. 397 (2022).

[22] S. Ndao, Y. Peles, M.K. Jensen, Experimental investigation of flow boiling heat transfer of jet impingement on smooth and micro structured surfaces, Int. J. Heat Mass Transf. 55 (2012) 5093–5101.

[23] L. Qiu, S. Dubey, F.H. Choo, F. Duan, Confined jet impingement boiling in a chamber with staggered pillars, Appl. Therm. Eng. 131 (2018) 724–733.

[24] W. Wana, D. Deng, Q. Huang, T. Zeng, Y. Huang, Experimental study and optimization of pin fin shapes in flow boiling of micro pin fin heat sinks, Appl. Therm. Eng. 114 (2017) 436–449.

[25] R. Jenkins, R. Lupoi, R. Kempers, A.J. Robinson, Heat transfer performance of boiling jet array impingement on micro-grooved surfaces, Exp. Therm Fluid Sci. 80 (2017) 293–304.

[26] S. Narumanchi, A. Troshko, D. Bharathan, V. Hassani, Numerical simulations of nucleate boiling in impinging jets: Applications in power electronics cooling, Int. J. Heat Mass Transf. 51 (2008) 1–12.

[27] S. Abishek, R. Narayanaswamy, V. Narayanan, Effect of heater size and Reynolds number on the partitioning of surface heat flux in subcooled jet impingement boiling, Int. J. Heat Mass Transf. 59 (2013) 247–261.

[28] K. Esmailpour, A. Azizi, S.M. Hosseinalipour, Numerical study of jet impingement subcooled boiling on superheated surfaces, Sci. Iran. 26 (2019) 2369–2381.

[29] L. Qiu, S. Dubey, F.H. Choo, F. Duan, Effect of conjugation on jet impingement boiling heat transfer, Int. J. Heat Mass Transf. 91 (2015) 584–593.

[30] D. Wright, K.J. Craig, J.P. Meyer, Computational investigation of single and multi-jet array impingement boiling, Appl. Therm. Eng. 218 (2023).

[31] S.E. Kim and D. Choudhury, A near-wall treatment using wall functions sensitized to pressure gradient. *The American Society of Mechanical Engineers*, 1995. **2017**.

[32] ANSYS, *Ansys Fluent Theory Guide*. 2022.

[33] M.H. Rausch, L. Kretschmer, S. Will, A. Leipertz, A.P. Fröba, Density, Surface Tension, and Kinematic Viscosity of Hydrofluoroethers HFE-7000, HFE-7100, HFE-7200, HFE-7300, and HFE-7500, J. Chem. Eng. Data 60 (2015) 3759–3765.

[34] ANSYS, *Ansys Fluent User's guide*. 2022.

[35] H.K. Versteeg, W. Malalasekera, An introduction to computational fluid dynamics, Second Edition ed., Pearson Education Limited, Glasgow, 2007.

[36] J. Bi, K. Vafai, D.M. Christopher, Heat transfer characteristics and CHF prediction in nanofluid boiling, Int. J. Heat Mass Transf. 80 (2015) 256–265.

[37] K. Esmailpour, A. Azizi, S.M. Hosseinalipour, Numerical study of jet impingement subcooled boiling on superheated surfaces, Sci. Iran. 26 (B) (2019) 2369–2381.

[38] A. Tomiyama, Struggle with computational bubble dynamics, Multiph. Sci. Technol. 10 (1998) 369–405.

[39] S.P. Antal, R.T. Lahey, J.E. Flaherty, Analysis of phase distribution in fully developed laminar bubbly two-phase flow, Int. J. Multiph. Flow 17 (1991) 635–652.

[40] M. Lopez de Bertodano, R.T. Lahey, O.C. Jones, Turbulent bubbly two-phase flow data in a triangular duct, Nucl. Eng. Des. 146 (1994) 43–52.

[41] A.A. Troshko, Y.A. Hassan, A two-equation turbulence model of turbulent bubbly flows, Int. J. Multiph. Flow 27 (2001) 1965–2000.

[42] V.H. Del Valle, D.B.R. Kenning, Subcooled flow boiling at high heat flux, Int. J. Heat Mass Transf. 28 (1985) 1907–1920.

[43] R. Cole, A photographic study of pool boiling in the region of the critical heat flux, Am. Inst. Chem. Eng. (1960) 538.

[44] E. Krepper, R. Rzehak, CFD for subcooled flow boiling: Simulation of DEBORA experiments, Nucl. Eng. Des. 241 (2011) 3851–3866.

[45] M. Lemmert and L.M. Chawla, Influence of flow velocity on surface boiling heat transfer coefficient in heat transfer in boiling. *Academic Press and Hemisphere*, 1977.

[46] H.C. Unal, Maximum bubble diameter, maximum bubble-growth time and bubble-growth rate during the subcooled nucleate flow boiling of water up to 17.7 mn/m2, Int. J. Heat Mass Transf. 19 (1975) 643–649.